

Cold gas in cluster cores: Global stability analysis and non-linear simulations of thermal instability

Prakriti Pal Choudhury [†], Prateek Sharma [‡]

[†] Department of Physics, Indian Institute of Science, Bangalore, India 560012 (prakriti@physics.iisc.ernet.in)

[‡] Department of Physics and Joint Astronomy Program, Indian Institute of Science, Bangalore, India 560012 (prateek@physics.iisc.ernet.in)

17 September 2018

ABSTRACT

We perform global linear stability analysis and idealized numerical simulations in global thermal balance to understand the condensation of cold gas from hot/virial atmospheres (coronae), in particular the intracluster medium (ICM). We pay particular attention to geometry (e.g., spherical versus plane-parallel) and the nature of the gravitational potential. Global linear analysis gives a similar value for the fastest growing thermal instability modes in spherical and Cartesian geometries. Simulations and observations suggest that cooling in halos critically depends on the ratio of the cooling time to the free-fall time ($t_{\text{cool}}/t_{\text{ff}}$). Extended cold gas condenses out of the ICM only if this ratio is smaller than a threshold value close to 10. Previous works highlighted the difference between the nature of cold gas condensation in spherical and plane-parallel atmospheres; namely, cold gas condensation appeared easier in spherical atmospheres. This apparent difference due to geometry arises because the previous plane-parallel simulations focussed on *in situ* condensation of multiphase gas but spherical simulations studied condensation *anywhere* in the box. Unlike previous claims, our nonlinear simulations show that there are only minor differences in cold gas condensation, either *in situ* or *anywhere*, for different geometries. The amount of cold gas depends on the shape of $t_{\text{cool}}/t_{\text{ff}}$; gas has more time to condense if gravitational acceleration decreases toward the center. In our idealized plane-parallel simulations with heating balancing cooling in each layer, there can be significant mass/energy/momentum transfer across layers that can trigger condensation and drive $t_{\text{cool}}/t_{\text{ff}}$ far beyond the critical value close to 10.

Key words: galaxies: halos – galaxies: cooling flows – instabilities – methods: numerical.

1 INTRODUCTION

Galaxy formation in dark matter haloes is understood to be a consequence of the combined effects of cooling, heating, and gravity (e.g., see White & Frenk 1991; Springel et al. 2005; Bower et al. 2006). Gas does not simply cool out of the hot virialized intracluster medium (ICM), but is maintained in rough thermal balance due to energy input by active galactic nucleus (AGN) jets in cores of galaxy clusters (McNamara & Nulsen 2007).

Observations show that the galaxy cluster cores with short cooling times or small core entropies have spatially extended multiphase gas and current star formation (Rafferty, McNamara & Nulsen 2008; Cavagnolo et al. 2009; McDonald et al. 2010). Recent theoretical and computational works, beginning with idealized simulations of local thermal instability in global thermal balance (McCourt et al. 2012; Sharma et al. 2012b) and culminating with the simulations of feedback-driven AGN jets interacting with the ICM (Gas-

pari, Ruszkowski & Sharma 2012; Li & Bryan 2014; Prasad, Sharma & Babul 2015), have shown that cold gas condenses out of the ICM if the ratio of cooling time to the free-fall time ($t_{\text{cool}}/t_{\text{ff}}$) is $\lesssim 10$. Moreover, cool cluster cores with jet feedback show heating and cooling cycles in which this ratio ($\min[t_{\text{cool}}/t_{\text{ff}}]$) varies from a few to few tens (Prasad, Sharma & Babul 2015; Li et al. 2015). A rough floor of $t_{\text{cool}}/t_{\text{ff}} \approx 10$ has been recently confirmed in observations of halos with temperatures ranging from 0.5 to 15 keV (Voit et al. 2015). The interpretation is that AGN feedback, fueled by condensing cold gas, kicks in for a shorter cooling time and reheats the hot phase such that $t_{\text{cool}}/t_{\text{ff}} \gtrsim 10$ everywhere.

Idealized simulations of hot ICM in global thermal balance, confined by the dark matter potential, have shown that the initial ratio of cooling time to free-fall time has to be less than a critical value (close to 10) if *extended* cold gas has to condense out of the hot ICM (Sharma et al. 2012b); cold gas does not appear for a larger $t_{\text{cool}}/t_{\text{ff}}$ even if we wait

arXiv:1512.01217v2 [astro-ph.GA] 20 Jan 2016

for a long time. In contrast, a recent study based on idealized simulations, with a constant ratio of cooling-time to free-fall time throughout, suggests that the initial $t_{\text{cool}}/t_{\text{ff}}$ determines the onset time of cold gas formation but cold gas condenses eventually if one waits long enough (Meece, O’Shea & Voit 2015). We critically examine this issue in our paper, and show that the authors’ claim is a trivial consequence of gravity vanishing in the midplane of their simulations. In other words, gravitational acceleration vanishes at the midplane, and hence gravity cannot suppress cold gas condensation there. As we show later, fluctuations generated due to local thermal instability at the midplane can lead to cold gas far from there.

Meece, O’Shea & Voit (2015) also highlighted that there is not much dependence on geometry (e.g., plane-parallel versus spherical) of cold gas condensation from virial atmospheres. Prior to this, it was believed that it is much easier for cold gas to condense in spherical geometry as compared to a plane-parallel atmosphere. Multiphase gas was claimed to condense out if $\min(t_{\text{cool}}/t_{\text{ff}}) \lesssim 10$ (more precisely, $t_{\text{TI}}/t_{\text{ff}}$,¹ the ratio of local thermal instability growth-time and free-fall time) in spherical geometry (Sharma et al. 2012b) and $\lesssim 1$ in a plane-parallel atmosphere (McCourt et al. 2012). This anomaly of a factor of 10 has been argued to be the effect of geometric compression in spherical geometry, which makes it easier to form cold gas. Experiments with a phenomenological compression term to simulate the geometric effect in a simple blob model (motivated by Pizzolato & Soker 2005), have shown that the formation of cold gas may be triggered for $t_{\text{TI}}/t_{\text{ff}} \lesssim 10$ (Singh & Sharma 2015). Our reanalysis of numerical simulations confirms that geometry does not play an important role in predicting the onset of cold gas condensation. Sharma et al. (2012b) and McCourt et al. (2012) found a dependence on geometry because the former concentrated on condensation *anywhere* in the computational domain, whereas latter focussed on *in situ* condensation (i.e., condensation in the plane where $t_{\text{TI}}/t_{\text{ff}}$ is minimum) of multiphase gas.

Given the importance of cold gas condensation in hot coronae, in this paper we combine global linear stability analysis and idealized numerical simulations to have a definitive say on the properties of the *extended* cold gas condensing out of the hot atmosphere. The paper is divided into two main parts: a global linear stability analysis and numerical simulations of local thermal instability in global thermal balance. Section 2 presents our physical setup and the equations that we solve. Section 3 describes the global linear stability analysis and section 4 is on results from numerical simulations. We conclude in section 5.

¹ While we can calculate $t_{\text{cool}} \equiv (3/2)nk_B T/n_e n_i \Lambda$ and $t_{\text{TI}} \equiv (10/9)t_{\text{cool}}$ (for a density/temperature independent constant heating rate; $[10/3]t_{\text{cool}}$ for a local heating rate linearly proportional to density; for details, see McCourt et al. 2012) in simulations, we do not know t_{TI} in cluster cores because we do not know the microscopic heating mechanism. Simulations with turbulent heating/mixing give a growth rate consistent with a heating rate density independent of density, as required to match observations (Banerjee & Sharma 2014).

2 PHYSICAL SETUP

In this section we describe the physical setup that we use to study the evolution of local thermal instability in an atmosphere satisfying global thermal equilibrium. This is a useful model to understand the origin of multiphase gas in galaxy cluster cores. The same basic setup is used for the global thermal instability analysis in section 3 and for idealized numerical simulations in section 4.

2.1 Model & equations

The background/unperturbed ICM is in hydrostatic and thermal equilibrium. The equations governing the evolution of gas in the ICM are

$$\frac{D\rho}{Dt} = -\rho\nabla \cdot \mathbf{v}, \quad (1)$$

$$\frac{D\mathbf{v}}{Dt} = -\frac{1}{\rho}\nabla p - g\hat{\mathbf{r}}, \quad (2)$$

$$\frac{p}{(\gamma-1)} \frac{D}{Dt} \left[\ln \left(\frac{p}{\rho^\gamma} \right) \right] = -q^-(n, T) + q^+(r, t), \quad (3)$$

where D/Dt is the Lagrangian derivative, ρ , \mathbf{v} and p are mass density, velocity and pressure; $\gamma = 5/3$ is the adiabatic index; $q^-(n, T) \equiv n_e n_i \Lambda(T)$ ($n_e \equiv \rho/[\mu_e m_p]$ and $n_i \equiv \rho/[\mu_i m_p]$ are electron and ion number densities, respectively; $\mu_e = 1.17$, $\mu_i = 1.32$, and m_p is proton mass) and $q^+(r, t) \equiv \langle q^- \rangle$ (this ansatz imposes thermal balance in shells), $\Lambda(T)$ is the temperature-dependent cooling function, and angular brackets indicate shell averaging. The background hydrostatic equilibrium implies $dp_0/dr = -\rho_0 g$, where a subscript ‘0’ refers to equilibrium quantities and acceleration due to gravity $g \equiv d\Phi/dr$ (Φ is the fixed gravitational potential). The background quantities are functions of r and the perturbations, in general, depend on all coordinates and time.

Our global linear stability analysis in section 3 is solved as a linear eigenvalue problem in radius. All perturbed quantities (density, velocity, etc.) are expanded in a Chebyshev polynomial basis, and the matrix equation for eigenvalues and eigenfunctions is solved numerically. For numerical simulations in section 4 we simply initialize isobaric density perturbations and study their evolution; strict thermal equilibrium in shells ($q^+ = \langle q^- \rangle$) is maintained at all times.

2.2 Gravitational acceleration profiles

For most of our runs we use the NFW profile for the potential and gravitational acceleration,

$$\Phi_{\text{NFW}} = -\frac{GM_{200} \ln(1 + c_{200}r/r_{200})}{[\ln(1 + c_{200}) - c_{200}/(1 + c_{200})]r}, \quad (4)$$

$$g_{\text{NFW}} = \frac{d}{dr}\Phi_{\text{NFW}}, \quad (5)$$

where $M_{200} = 5.24 \times 10^{14} M_\odot$ is the dark matter halo mass within r_{200} and r_{200} is the approximate virial radius (Navarro, Frenk & White 1996), within which the mean density is 200 times the critical density of the universe ($9.2 \times 10^{-30} \text{ g cm}^{-3}$), and $c_{200} = 3.3$ is the concentration parameter. While the NFW potential is normally used only in spherical geometry, we also use it in Cartesian/plane-parallel setups in which the gravitational potential and acceleration

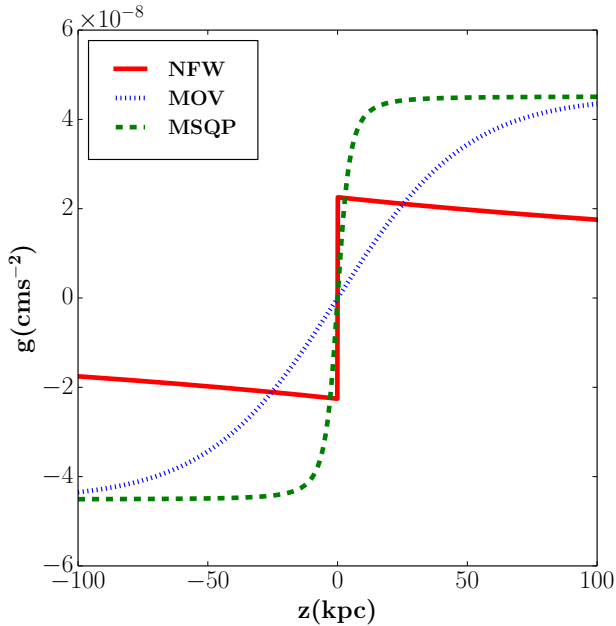


Figure 1. Different gravitational acceleration profiles that we use (Eqs. 5-7) as a function of distance from the midplane (or the center, in case of spherical geometry).

have the same dependence on $|z|$. This is done to compare cold gas condensation in spherical and plane-parallel geometries.

In order to compare with previous idealized simulations (e.g., McCourt et al. 2012; Meece, O’Shea & Voit 2015), especially the influence of the form of gravity on cold gas condensation, we also perform runs with the following gravitational accelerations

$$g_{\text{MOV}}(r) = g_0 \tanh\left(\frac{r}{r_s}\right), \quad (6)$$

$$g_{\text{MSQP}}(r) = g_0 \frac{r/r_s}{(1 + [r/r_s]^2)^{\frac{1}{2}}}, \quad (7)$$

where r_s is a scale height (chosen 5 kpc for MSQP and 50 kpc for MOV; for the same r_s , the shapes of the two accelerations are very similar). Note that r is simply replaced by z for plane-parallel atmospheres.

In order to make meaningful comparisons with the realistic NFW profiles, we take the value of g_0 such that the order of magnitude of gravitational acceleration is similar to that of the realistic NFW gravity. We also carry out idealized MSQP numerical simulations in which $g_0 = 1$. Although the magnitude of gravitational accelerations is similar, their spatial dependence is different; in particular, gravity becomes weaker toward the center for MSQP and MOV gravities (Fig. 1). Note that at small radii $g \propto r$ for MOV and MSQP gravities, and thus $t_{\text{ff}} = (2r/g)^{1/2}$ is approximately a constant and $t_{\text{cool}}/t_{\text{ff}}$ peaks at the center because of the highest density at the center. In contrast, $t_{\text{cool}}/t_{\text{ff}}$ peaks at ~ 10 kpc for a realistic NFW gravity (c.f. Fig. 7).

2.3 Equilibrium profile

The entropy profile of the ICM in initial hydrostatic equilibrium is modeled by

$$K(r) = \frac{T_{\text{keV}}}{n_e^{\gamma-1}} = K_0 + K_{100} \left(\frac{r}{r_{100}}\right)^\alpha, \quad (8)$$

where $r_{100} = 100$ kpc; we choose $K_{100} = 80$ keV cm² for all runs and linear analysis (Cavagnolo et al. 2009). The core entropy value K_0 is varied to obtain various $t_{\text{TI}}/t_{\text{ff}}$ profiles in numerical simulations. In global linear stability analysis (section 3), we choose $K_0 = 8$ keV cm² for NFW gravity and $K_0 = 23$ keV cm² for MOV gravity (this choice gives a similar $\min[t_{\text{TI}}/t_{\text{ff}}] \approx 7.3$). The equilibrium profiles are obtained as a function of the radial distance from the center (r ; or distance from the midplane $[z]$ in case of a plane-parallel atmosphere) by assuming hydrostatic equilibrium in the external potential well (NFW, MSQP, or MOV). The electron number density at 100 kpc is 0.00875 cm⁻³. The outer ICM electron density combined with the entropy profile and hydrostatic equilibrium completely specify the ICM profiles.

In addition to the MOV and MSQP gravitational field with realistic entropy profiles (Eq. 8), we carry out some idealized MSQP (isothermal and isentropic, with profiles given by Eqs. 9 & 10 of McCourt et al. 2012; see Table 2) runs to compare with previous simulations.

2.4 Idealized heating and cooling

We use a fit to the plasma cooling function with a third of the solar metallicity, given by Eq. 12 and the solid line in Fig. 1 of Sharma, Parrish & Quataert (2010); idealized MSQP runs use a cooling function $\Lambda = \Lambda_0 T^{1/2}$ (see Table 2). Since the cluster core plasma appears to be in rough thermal balance, we adopt an *idealized* heating function such that r/z -dependent heating rate at every radius/height and at all times is equal to the average cooling rate at the same height; i.e., $q^+ \equiv \langle n_e n_i \Lambda(T) \rangle$, where angular brackets represent shell averaging. Note that our heating rate per unit volume is independent of the local density and temperature.

In the plane-parallel numerical simulations, we have excluded heating and cooling in the region -1 kpc $\leq z \leq 1$ kpc because gravity necessarily vanishes at the midplane, where cooling overdense blobs are not affected by gravity, and local thermal instability inevitably leads to multiphase gas within a few cooling times, irrespective of $t_{\text{TI}}/t_{\text{ff}}$.² Moreover, we are mainly concerned about *extended* cold gas filaments observed in cool cluster cores. As we note in section 4.5, allowing thermal-instability generated multiphase gas in the midplane can artificially enhance condensation beyond the midplane even in atmospheres with large $t_{\text{TI}}/t_{\text{ff}}$.

2.5 Important timescales

In this section we define the important timescales relevant to our setup of local thermal instability in global thermal equilibrium. Since $t_{\text{cool}}/t_{\text{ff}}$ or $t_{\text{TI}}/t_{\text{ff}}$ plays a crucial role in cold gas formation, we define the thermal instability (TI)

² We do not have to turn off cooling and heating within 1 kpc in spherical ICM runs because the central region is excised for these.

time-scale (the inverse of the local exponential growth rate for a constant heating rate per unit volume)

$$t_{\text{TI}} = \frac{\gamma t_{\text{cool}}}{(2 - d \ln \Lambda / d \ln T)}, \quad (9)$$

where

$$t_{\text{cool}} = \frac{nk_B T}{(\gamma - 1)n_e n_i \Lambda}. \quad (10)$$

For free-free cooling (with $\Lambda \propto T^{1/2}$) relevant to clusters, $t_{\text{TI}} = (10/9)t_{\text{cool}}$. The free-fall time

$$t_{\text{ff}} = \left(\frac{2r}{g}\right)^{1/2}, \quad (11)$$

where $g(r)$ (r is replaced by z for plane-parallel atmospheres) is the gravitational acceleration at the radius of interest.

3 LINEAR STABILITY ANALYSIS: GLOBAL MODES

While the local WKB analysis of thermal instability in global thermal and dynamical equilibrium is well-known (Field 1965), we carry out a global linear analysis of our equilibrium set up, focusing on the growing (strictly speaking, overstable, which is both growing and oscillating) thermal instability modes. Linear analysis of thermal instability in cluster cooling flows has a long history (e.g., Malagoli, Rosner & Bodo 1987; Balbus 1988; Balbus & Soker 1989; Kim & Narayan 2003). For an equilibrium with a background flow, Lagrangian analysis appears more reliable (Balbus 1988; Balbus & Soker 1989) but as we explain in the next paragraph, a static background is a better description of cool cluster cores. For the cluster cores in rough thermal balance there is no background flow and the Eulerian and Lagrangian approaches (for both local and global analyses) are equivalent (see the discussion after Eq. 31 in Kim & Narayan 2003).

Recent results have shed new light on thermal equilibrium in galaxy cluster cores, in particular the role of AGN feedback in providing rough *global* thermal balance and the lack of massive cooling flows. Moreover, now it is clear that the anisotropic nature of thermal conduction prevents it from playing a dominant role in global thermal balance (Parrish, Quataert & Sharma 2009; Wagh, Sharma & McCourt 2014 and references therein). Therefore, in this paper we study the nature of global thermal instability with a background equilibrium (both thermal and hydrostatic) state which is consistent with these recent advances; i.e., we neglect thermal conduction and an equilibrium inflow (these assumptions make the analysis more tractable; the observed multiphase inflow is small and is due to the nonlinear evolution of local thermal instability), and assume global thermal balance ($q^+ = \langle q^- \rangle$).

One of the reasons we carry out a global linear instability analysis in spherical geometry and compare it with the same analysis in a plane-parallel atmosphere is to see if the *apparent*³ result, that it is easier for cold gas to condense out of the hot ICM in spherical geometry compared to a

plane-parallel geometry, can be due to a higher growth rate (equivalently, a shorter growth time) in spherical geometry because of geometrical compression as an over dense blob falls in toward the center. The evolution of overdensity, assuming a linear growth timescale t_{TI} and a nonlinear mixing time τ_{nl} , is roughly described by

$$\frac{d\delta}{dt} \approx \frac{\delta}{t_{\text{TI}}} - \frac{\delta^2}{\tau_{\text{nl}}},$$

which for the amplitude in saturated state gives $\delta_{\text{sat}} \approx \tau_{\text{nl}}/t_{\text{TI}}$. Thus, the saturated amplitude is inversely proportional to linear growth time. A shorter t_{TI} can, in principle, lead to higher overdensities and easier condensation of cold gas in spherical geometry.

In fact, based on this anticipation, Singh & Sharma (2015) erroneously (it appears in light of the global results in this paper) introduced a linear term ($-2g/r$ term in Eq. 24 of their paper) that leads to a larger instability rate in spherical geometry compared to a plane-parallel atmosphere. Our global linear instability analysis can easily reveal any difference in the growth rate of thermally unstable local and global modes. Our results show that there is no substantial difference between the linear growth rates in Cartesian and spherical atmospheres (c. f. Fig. 6). This is consistent with nonlinear simulations of section 4, which show only minor differences between the threshold $t_{\text{TI}}/t_{\text{ff}}$ for cold gas condensation in spherical and plane-parallel atmospheres.

We assume that the time dependence of all perturbations (denoted by a subscript 1) is given by $e^{\sigma t}$, where σ is the growth rate of the mode (it is an imaginary number for purely oscillating modes). The linearized equations for perturbations (in spherical coordinates; generalization to a plane parallel atmosphere is straightforward) are

$$\begin{aligned} \sigma \rho_1 + \frac{1}{r^2} \frac{\partial}{\partial r} (r^2 \rho_0 v_{r1}) + \frac{\rho_0}{r \sin \theta} \frac{\partial}{\partial \theta} (\sin \theta v_{\theta 1}) \\ + \frac{\rho_0}{r \sin \theta} \frac{\partial}{\partial \phi} v_{\phi 1} = 0, \end{aligned} \quad (12)$$

$$\sigma \rho_0 v_{r1} = -\frac{\partial p_1}{\partial r} - \rho_1 g, \quad (13)$$

$$\sigma \rho_0 v_{\theta 1} = -\frac{1}{r} \frac{\partial p_1}{\partial \theta}, \quad (14)$$

$$\sigma \rho_0 v_{\phi 1} = -\frac{1}{r \sin \theta} \frac{\partial p_1}{\partial \phi}, \quad (15)$$

$$\sigma \frac{s_1}{s_0} + \frac{\gamma N^2 v_{r1}}{g} = \frac{-1}{t_{\text{cool}0}} \left[2 \frac{\rho_1}{\rho_0} + \frac{d \ln \Lambda}{d \ln T} \frac{T_1}{T_0} \right] \quad (16)$$

where $T_1/T_0 = p_1/p_0 - \rho_1/\rho_0$,

$$N^2 \equiv \frac{g}{\gamma} \frac{d}{dr} \ln \left(\frac{p_0}{\rho_0^\gamma} \right) \quad (17)$$

is the local Brunt-Väisälä (BV) frequency, and $t_{\text{cool}0} \equiv p_0 / \{[\gamma - 1] n_0^2 \Lambda(T_0)\}$ is the local cooling time. We have also defined a pseudo-entropy as $s \equiv p/\rho^\gamma$ such that $s_1/s_0 = p_1/p_0 - \gamma \rho_1/\rho_0$. The expression on the right hand side of

plane-parallel atmospheres. This is also pointed out by Meece, O'Shea & Voit (2015). This confusion arose as the plane-parallel simulations of McCourt et al. (2012) focused on *in situ* condensation of cold gas, whereas the spherical simulations of Sharma et al. (2012b) concerned with condensation *anywhere* outside of 1 kpc, not necessarily *in situ* at ~ 10 kpc where $t_{\text{TI}}/t_{\text{ff}}$ is minimum.

³ As we show later, using numerical simulations, that there is not much difference between condensation of cold gas in spherical and

Table 1. Global linear stability analysis models with axisymmetric perturbations

Gravity	Parameters	K_0 (keV cm ²)	$\min(t_{\text{TI}}/t_{\text{ff}})$	$\min(\sigma_{\text{real}}^{-1})$ (Gyr)	t_{TI} at $\min(t_{\text{TI}}/t_{\text{ff}})$ (Gyr)	t_{TI} at N_{max} (Gyr)
spherical, Cartesian, NFW	$k_x r_{\text{out}} = 100$	8	7.3	0.57	0.36	0.22
global spherical harmonics, NFW	$l = 10$	8	7.3	0.446	0.36	0.22
global spherical harmonics, NFW	$l = 2$	8	7.3	0.448	0.36	0.22
spherical, Cartesian, MOV	$k_x r_{\text{out}} = 100$	23	7.3	3.8	0.61	1.84

Notes: In all cases, the fastest growth timescale ($\sigma_{\text{real}}^{-1}$) for resolved modes is longer than the local thermal instability timescale.

Eq. 16 assumes that $q_1^+ = 0$. The perturbed heating rate density q_1^+ is zero if $\partial/\partial\theta$ or $\partial/\partial\phi$ is non-zero (from our assumption of thermal balance in shells). Otherwise, q_1^+ depends on our assumption: $q_1^+ = q_1^-$ if we assume thermal balance in shells at all times (even for perturbations; as in our simulations discussed in section 4); $q_1^+ = 0$ is also a valid choice as thermal balance is only required to be maintained in equilibrium.

Eqs. 12-16 are in the form of an eigenvalue problem. In absence of cooling and heating, these equations describe the coupled sound and internal gravity waves.⁴ These waves are essentially decoupled when the two frequencies are very different (i.e., in the usual Boussinesq approximation). With cooling and heating, both the internal gravity waves and sound waves can have growing or damped solutions, depending on the perturbed generalized heat loss function $q^- - q^+$ (Eq. 3). For local modes with short sound crossing times compared to the cooling time the perturbation is usually evaluated in isobaric (isentropic) approximation for internal gravity waves (sound waves; Field 1965). For our cooling function ($\Lambda[T]$), only the internal gravity waves show growing modes. Since our method does not make Boussinesq approximation, our global method calculates exact oscillation frequencies/growth rates; our linear growth/oscillation rates match local results in appropriate limits.

Appendix A gives the local and global forms of the linearized equations (Eqs. 12-16) after separating dependent variables in the three directions. We solve the global eigenvalue problem numerically by employing a pseudospectral method (Boyd, J. P. 2000). The coupled first-order linear equations are converted into a matrix eigenproblem. We de-dimensionalize the problem by scaling density and pressure with their values ($p_0[r_{\text{in}}]$, $\rho_0[r_{\text{in}}]$) at the inner radius $r_{\text{in}} = 0.1$ kpc; velocities are scaled by $c_0 \equiv (p_0[r_{\text{in}}]/\rho_0[r_{\text{in}}])^{1/2}$. All lengths are scaled by the outer radius $r_{\text{out}} = 100$ kpc. We find that the numerical eigen-solver is more robust if we de-dimensionalize the equations. Appendix B discusses the pseudospectral method in detail.

Boundary conditions: The four first-order equations (Eqs. A1-A4 for local analysis or A5-A8 for global analysis in the transverse direction) require as many boundary conditions in general. A quick glance at Eqs. A1-A4 sug-

gests that the eigenvalues are degenerate for global spherical modes with different m . The radial domain $[r_{\text{in}}, r_{\text{out}}]$ is mapped to $-1 \leq \xi \leq 1$, in order to apply the pseudospectral method (see Appendix B). We assume no penetration through the outer radial direction ($v_{r1} = 0$ at $r = r_{\text{out}}$ or $\xi = 1$). The other boundary conditions are $v_{\theta 1} = 0$ at $\xi = 1$, $dv_{\theta 1}/d\xi = 0$ at $\xi = -1$ ($r = r_{\text{in}}$), and $s_1 = 0$ at $\xi = -1$. We get similar results for other reasonable boundary conditions. The pseudospectral method is known to be extremely sensitive to the boundary conditions. Therefore, we chose our boundary conditions only after ensuring the convergence of eigenvalues and eigenmodes.

3.1 Eigenvalues and numerical convergence

Figure 2 shows numerical eigenvalues of the overstable (with a positive real σ) internal gravity modes, destabilized by thermal instability. More modes converge, and the eigenvalues fall on top of each other, as we increase the resolution. We only show the unstable modes; the sound wave is also affected by cooling and heating, but is damped (with a negative real part of σ) as the modes are effectively isentropic (Field 1965). The physical modes show convergence with an increasing n (number of Chebyshev polynomials or the G-L grid points in the eigenfunction expansion; see Eq. B1). The other modes are either physically spurious or unresolved. We only focus on the resolved modes. To compare with local results, in Figure 2 the growth rate (real part of σ) is scaled with t_{TI} at $\min(t_{\text{TI}}/t_{\text{ff}})$ in the equilibrium profile and the oscillation frequency (imaginary part of σ) is scaled with the maximum value of the BV frequency.

Figure 3 shows the overstable internal gravity modes in a fully-global analysis in spherical geometry (taking a spherical harmonic basis function; Eqs. A1-A4). The value of l is such that the transverse wavenumber is similar to the local analysis (Eqs. A5-A8) shown in Figure 2. The growth rates of the fastest growing overstable modes in the global analysis are only slightly higher than the local analysis. Therefore, we conclude that there is only a minor difference between the growth rates in global and local analyses. This is also verified for the truly global $l = 2$ mode (see Table 1).

3.2 Local and global gravity modes

Assuming that the modes vary as $e^{(\sigma t + i\mathbf{k}\cdot\mathbf{x})}$ ($\mathbf{k} = \hat{\mathbf{x}}k_x + \hat{\mathbf{z}}k_z$ is the wavenumber), the local ($|k|H \gg 1$, H is the entropy/pressure scale height) dispersion relation (using Eqs.

⁴ In absence of gravity, the only direction in the homogeneous isotropic equilibrium is along the wavenumber \mathbf{k} . Thus, the modes in this case are the two oppositely propagating sound waves, and one entropy mode with $\sigma = 0$ and only non-zero density and temperature perturbations. With gravity, \mathbf{g} and \mathbf{k} define a plane ($x - z$ plane, assuming $\mathbf{k} \cdot \mathbf{g} \neq 0$) and we obtain two internal gravity modes in addition to sound waves.

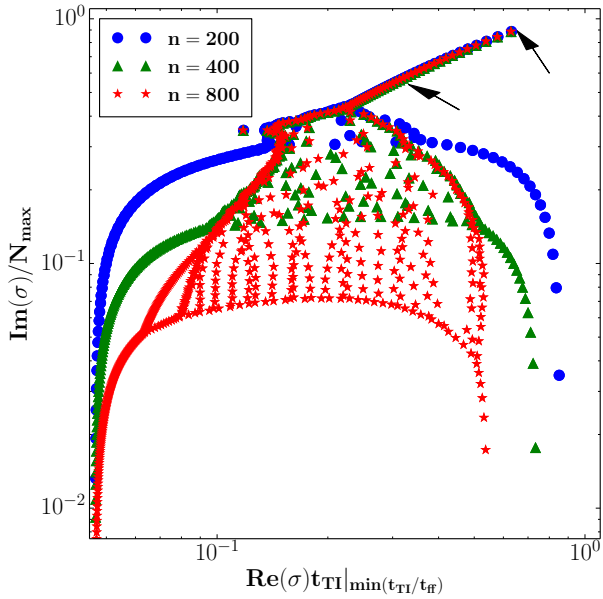


Figure 2. Convergence of eigenvalues of Eqs. A5 to A8, for different resolutions ($n = 200, 400, 800$) for our fiducial ICM confined by NFW gravity. The real part of the eigenvalue is normalized with N_{\max} and the imaginary part with t_{TI} evaluated at $\min(t_{\text{TI}}/t_{\text{ff}})$. For these runs, $k_x r_{\text{out}} = 100$. The arrows mark the eigenvalues for which the eigenmodes are shown in Figure 4. The fastest growing mode grows slightly slowly compared to the local growth rate at $\min(t_{\text{TI}}/t_{\text{ff}})$.

A5-A8) is given as

$$\sigma^4 + \frac{\sigma^3}{t_{\text{cool}}} \frac{d \ln \Lambda}{d \ln T} - \sigma^2 (i k_r g(r) - c_s^2 k^2) - \sigma \left(\frac{i k_r g(r)}{t_{\text{cool}}} \frac{d \ln \Lambda}{d \ln T} + \frac{c_s^2 k^2}{t_{\text{TI}}} \right) + N^2 k_x^2 c_s^2 = 0.$$

Assuming, $N, t_{\text{TI}}^{-1} \ll k c_s$ ($c_s \equiv [\gamma p_0 / \rho_0]^{1/2}$ is the local sound speed) the low frequency g-modes have a dispersion relation,

$$\sigma^2 - \frac{\sigma}{t_{\text{TI}}} + \frac{k_x^2}{k^2} N^2 = 0,$$

with the two roots being

$$\sigma = \frac{1}{2t_{\text{TI}}} \pm \frac{1}{2} \left(\frac{1}{t_{\text{TI}}^2} - \frac{4N^2 k_x^2}{k^2} \right)^{\frac{1}{2}}.$$

For $k_x = 0$, the $\sigma = 0$ solution is trivial (i.e., $\rho_1, v_{r1}, v_{\theta 1}, p_1 = 0$) in the local ($|k|H \gg 1$) limit. The $\sigma = t_{\text{TI}}^{-1}$ solution does not exist if heating balances cooling in shells ($q^+ = \langle q^- \rangle$ or $q_1^+ = q_1^-$, as in our set up), but exists as the local isobaric thermal instability if thermal balance does not hold for *perturbations* (e.g., if $q_1^+ = 0$, or in other words, if thermal balance is only imposed in equilibrium not on perturbations).⁵

⁵ Balbus (1988) has argued that there is no $k_x = 0$ (purely radial) isobaric thermally instability mode. However, linear analysis (Eqs. A5-A8) shows, as long as heating and cooling do not exactly balance in shells (i.e., $q_1^+ \neq q_1^-$), that it will exist as a

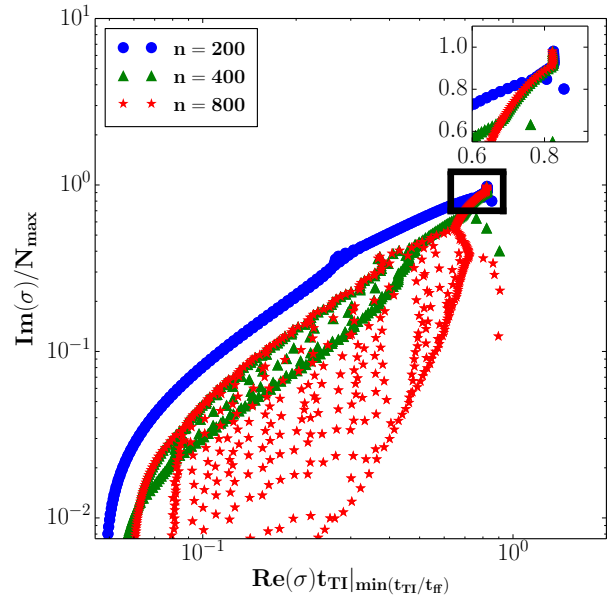


Figure 3. Convergence of eigenvalues for global linear analysis (Eqs. A1 to A4) of thermal instability, using different resolutions for our fiducial ICM confined by NFW gravity. The degree of spherical harmonic mode is $l = 10$ (corresponding to $k_x(r_{\text{out}})r_{\text{out}} \approx 10$). The inset shows the zoom-in on the converged modes. The growth rates are not substantially different from Figure 2.

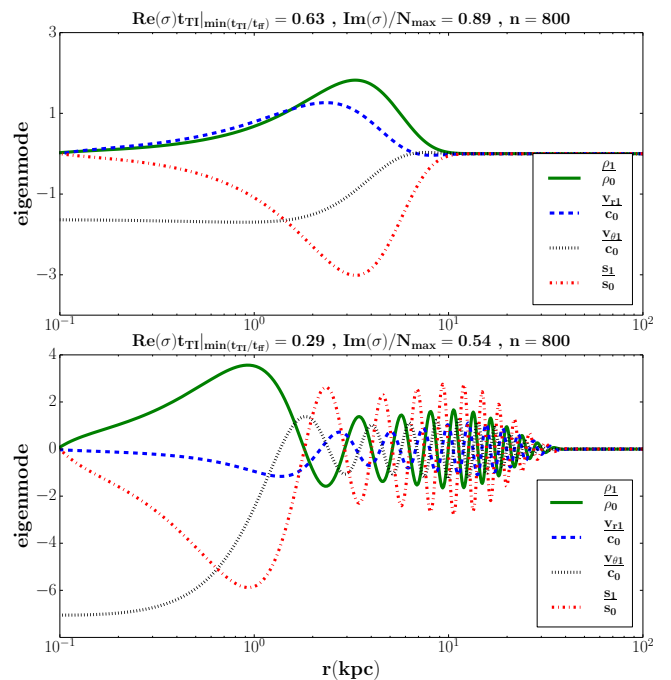


Figure 4. Eigenmodes for two different thermally unstable gravity modes with different eigenvalues, as indicated by arrows in Figure 2. We have verified that we obtain the same eigenmodes for different resolutions that show convergence for eigenvalues ($n = 200, 400, 800$ in Fig. 2).

Since the slowest varying mode in the r - direction (i.e., with lowest k_r) are the easiest to resolve, and they have the largest oscillation frequency of gravity modes ($\sigma \approx \pm ik_x N / [k_x^2 + k_r^2]^{1/2}$), the modes with the highest imaginary values of σ are resolved most easily (see Fig. 2). The profile of BV frequency (Eq. 17) for cool-core clusters is peaked toward the center and fall off at large radii (solid red line in Fig. 5). Therefore, the internal gravity modes become evanescent at large radii where $|\sigma_i| > N$, and the eigenmodes are confined to small radii in the center (e.g., Lufkin, Balbus & Hawley 1995). Gravity modes with a higher number of nodes and antinodes (i.e., higher k_r) have a smaller oscillation frequency, and hence are evanescent at larger radii. The two gravity eigenmodes shown in Figure 4 clearly illustrate this; a higher k_r corresponds to a smaller oscillation frequency and a more extended radial structure. As shown in Figure 5, the local BV frequency is peaked at larger radii for MOV gravity, therefore the resolved modes are confined at large radii (we have verified this) where the cooling time is long, and hence the growth rate is smaller (see Table 1 and red squares in Fig. 6).

3.3 Growth rates in plane-parallel and spherical atmospheres

Figure 6 compares the converged growth rates of thermally unstable internal gravity waves in spherical and plane parallel atmospheres for NFW and MOV gravities. It shows that there is no effect of geometry on the growth rate, unlike expected (e.g., Singh & Sharma 2015). Also note that the difference between spherical and plane-parallel atmospheres is slightly more for NFW gravity because the converged modes are centrally concentrated around $r = 0$ and truly global, whereas for MOV gravity the small radial wavenumber modes are confined over $\Delta r/r \lesssim 1$ close to N_{\max} and are essentially local.

4 NUMERICAL SIMULATIONS

Now that global stability analysis clearly shows that there are only minor differences in thermal instability growth rates in plane-parallel and spherical atmospheres, we turn to idealized 2-D/axisymmetric nonlinear numerical simulations to compare the two.

We perform 2-D axisymmetric simulations with both Cartesian (also referred to as ‘plane-parallel’) and spherical atmospheres (setup is described in section 4.1). While NFW gravity simulations are carried out in both plane-parallel and spherical geometries, simulations using MOV and MSQP gravities are only carried out in Cartesian geometries. A comparison of spherical and plane-parallel NFW simulations clearly shows that there is very little influence of geometry on the onset of cold gas condensation. In both geometries, in situ condensation requires a smaller $\min(t_{\text{cool}}/t_{\text{ff}})$ compared to condensation anywhere in the simulation box (section 4.2). The Cartesian NFW, MOV and MSQP simulations are used to test the influence of gravitational acceleration and

robust instability with purely growing modes with $\sigma = t_{\text{TI}}^{-1}$ and $p_1/p_0 \ll \rho_1/\rho_0$.

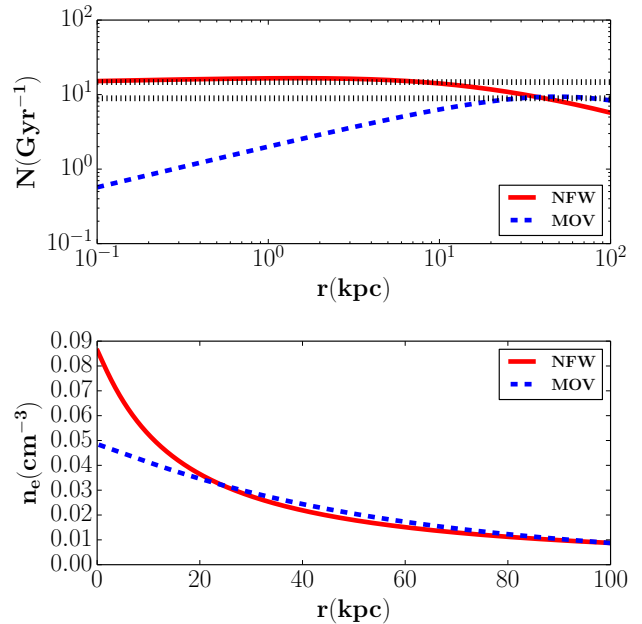


Figure 5. *Top panel:* The local BV frequency as a function of radius for NFW ($K_0 = 8 \text{ keV cm}^2$) and MOV ($K_0 = 23 \text{ keV cm}^2$) gravities. The horizontal dotted lines represent the imaginary part of the growth rate ($\sigma_i/N_{\max} = 0.89, 0.54$) for the modes shown in Figure 4. Eigenfunctions are confined to radii where $\sigma_i < N$ for both modes, as expected. Similarly, as expected from the shape of N versus r for MOV gravity, we verify that the lowest radial wavenumber modes are confined to $r \approx 60 \text{ kpc}$ (where N peaks). The BV frequency has a different profile for NFW and MOV gravities as it is proportional to the local gravitational acceleration, which is qualitatively different for the two cases (Figure 1). *Bottom panel:* The electron number density as a function of radius for NFW and MOV gravities.

density profiles (Eqs. 5–7) on cold gas condensation (section 4.4).

4.1 Simulation setup

We use the ZEUS-MP code (Hayes et al. 2006) to solve Euler equations with heating, cooling, and gravity (Eqs. 1–3). The initial condition consists of a hydrostatic equilibrium profile (described in section 2.3), superposed with isobaric small density perturbations. We also carry out simulations using different potential wells (NFW, MOV, MSQP; Eqs. 5–7) and different geometries (spherical & plane-parallel).

In addition to the runs with cluster-like parameters, we perform a few runs with the idealized setup similar to McCourt et al. (2012) (isothermal/isentropic corresponding to their Eqs. 9/10; these also use a $T^{1/2}$ cooling function cut off at $1/20$). Table 2 lists all our runs. Figure 7 shows the profiles of the ratio of the thermal instability timescale and the free fall time ($t_{\text{TI}}/t_{\text{ff}}$) in the unperturbed state of some of our model atmospheres (NFW, MOV, MSQP, and idealized MSQP). This ratio is important to interpret cold gas condensation in our setup.

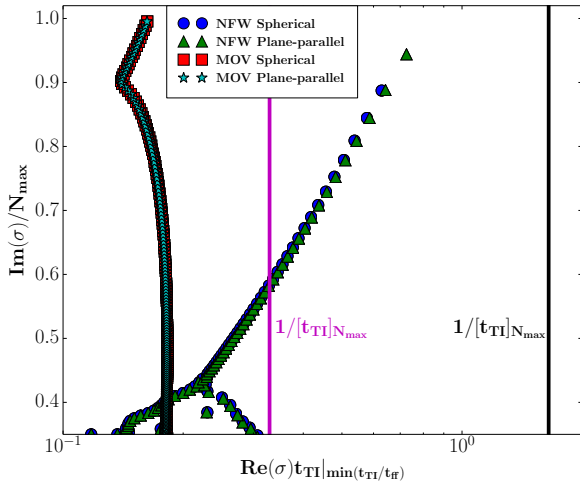


Figure 6. The converged thermally unstable internal gravity modes for spherical and plane-parallel atmospheres for NFW and MOV gravities. The only difference between spherical and plane-parallel gravities is that $(1/r^2)\partial/\partial r(r^2\rho_0 v_{r1})$ term in Eq. A5 is replaced by $\partial/\partial z(\rho_0 v_{z1})$. The growth rates for converged modes are almost equal (for MOV they coincide), suggesting that there is no effect of geometry on the linear growth rate. Here $n = 800$ and $k_x r_{\text{out}} = 100$. The vertical lines correspond to the local thermal instability growth rates (t_{TI}) measured at the peak of the local BV frequency (N_{max}). The magenta lines correspond to MOV gravity and black lines to NFW gravity. Note that the N_{max} peak for NFW gravity occurs close to the center where density is high, but for MOV gravity N_{max} it is further out where the density is much lower (Fig. 5).

4.1.1 Grids and geometries

The Cartesian runs have a resolution of 512×256 ($N_z \times N_x$), while the spherical runs have a resolution of 256×256 ($N_r \times N_\theta$). We have a comparable spatial resolution for the two geometries in the direction along gravity. The Cartesian grid runs from -100 kpc to 100 kpc in all three dimensions, while the spherical grid has the following range in the three directions: $1 \text{ kpc} \leq r \leq 100 \text{ kpc}$, $0 \leq \theta \leq \pi$ and $0 \leq \phi \leq 2\pi$.

The radial grid in spherical runs is logarithmic, with equal number of grid points from 1 to 10 kpc and 10 to 100 kpc. The Cartesian z -grid is partly logarithmic (-100 kpc to -1 kpc, 1 kpc to 100 kpc) and partly uniform (-1 kpc to 1 kpc), to match the resolution of the spherical simulations in the direction of gravity. Cartesian runs corresponding to MOV and MSQP gravities have a similar grid resolution. The idealized MSQP runs use a uniform grid throughout.

4.1.2 Initial and boundary conditions

For all runs we seed initial isobaric density perturbations such that the maximum $\delta\rho/\rho_0 \approx 0.3$ (the runs focusing on the early linear stage of thermal instability, shown in Fig. 10, use a smaller maximum amplitude of 0.01), where $\delta\rho = \rho - \rho_0$ and ρ_0 is the equilibrium density as a function of r (or z). The density fluctuations are isotropic and homogeneous (in

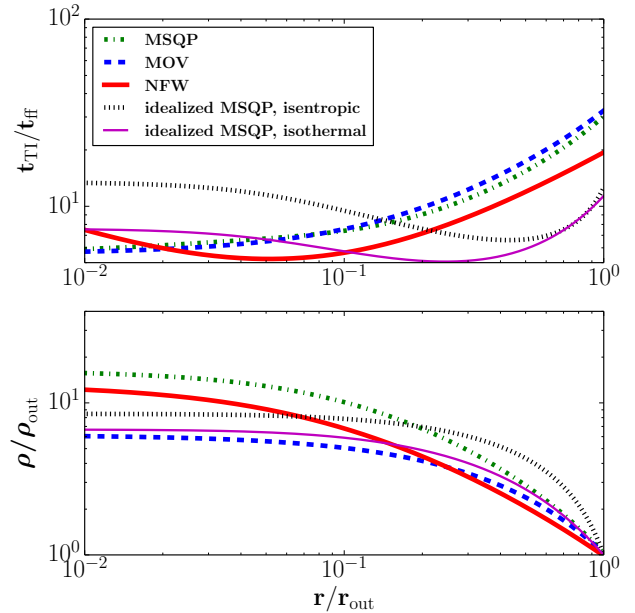


Figure 7. *Top panel:* The profiles of the ratio of the local thermal instability timescale and the local free-fall time ($t_{\text{TI}}/t_{\text{ff}}$) for various equilibrium atmospheres with $\min(t_{\text{TI}}/t_{\text{ff}}) \approx 5$: NFW, MOV, MSQP, and idealized MSQP (isothermal and isentropic). *Bottom panel:* The normalized gas density profiles for the same runs. While MSQP atmosphere uses Eq. 8 for the entropy profile, the idealized MSQP profiles are isothermal/isentropic and identical to Eq. 9/10 of McCourt et al. (2012). Also, while NFW and idealized MSQP profiles have a local minimum, the MOV and MSQP profiles have a minimum at the center.

the three dimensional Cartesian sense), given by

$$\frac{\delta\rho}{\rho_0} = \sum_{k,l,m} a_{k,l,m} \cos\left(\frac{2\pi(kx + ly + mz)}{r_{\text{out}}} + \phi_{k,l,m}\right),$$

where $\phi_{k,l,m}$ is the uniformly distributed random phase, the random mode amplitudes $a_{k,l,m}$ have a power spectrum $\propto (k^2 + l^2 + m^2)^{-1/2}$ for $2 \leq (|k|, |l|, |m|)r_{\text{out}}/2\pi \leq 10$, where $r_{\text{out}} = 100$ kpc is the outer radius. We choose the same mode amplitudes and phases for all spherical and plane-parallel runs, and therefore the density perturbations ($\delta\rho/\rho_0$) are identical in all our runs. This helps us make a precise comparison between our different runs.

At outer boundary the electron number density is fixed to be $n_{e,\text{out}} = 0.00875 \text{ cm}^{-3}$. For spherical simulations, the boundary conditions in the radial direction allow outflow at the inner boundary ($r_{\text{in}} = 1$ kpc) and inflow at the outer boundary ($r_{\text{out}} = 100$ kpc), with the density and internal energy density fixed to their equilibrium values at the outer boundary. The boundary conditions for θ and ϕ directions are, respectively, reflective/axisymmetric and periodic. For Cartesian runs we apply inflow boundary conditions at the two vertical boundaries (at $z = \pm 100$ kpc) and we fix the density and internal energy densities to their equilibrium values. We apply reflective boundary condition in x and y directions.

Table 2. List of idealized nonlinear simulations & their parameters

Gravity	K_0 (keV cm ²)	min($t_{\text{TI}}/t_{\text{ff}}$) (in equilibrium)	total $M_{\text{cold}}/M_{\text{tot}}^a$ [anywhere]	$M_{\text{cold}}/M_{\text{tot}}^b$ at min($t_{\text{TI}}/t_{\text{ff}}$) [in situ]	$r_{\text{cold,max}}$ (kpc)	runs till (Gyr)
spherical, NFW	2.0	2.6	.0016	0.12	24.4	15
	5.0	5.2	.0014	0.002	11.4	15
	8.0 [‡]	7.3	3.5×10^{-4}	2.1×10^{-4}	15.5	15
	10.0	8.6	2.2×10^{-4}	0.0	6.6	15
	20.0	13.6	0.0	0.0	-	15
	30.0	17.6	0.0	0.0	-	15
	45.0	22.5	0.0	0.0	-	15
Cartesian, NFW	2.0	2.6	0.09	0.123	13.5	15
	5.0	5.2	0.07 (0.08)	0.005 (0.006)	19.3 (19.3)	15 (10.9)
	8.0 [‡]	7.3	0.08 (0.09) (.12)	0.003 (0.004) (0.005)	9.9 (9.9) (9.9)	15 (10.9) (6.5)
	10.0	8.6	0.04 (0.05)	0.0 (0.0)	19.3 (19.3)	15 (10.9)
	20.0	13.6	0.03 (0.02)	10^{-5} (10^{-5})	17.68 (17.68)	15 (10.9)
	30.0	17.6	.02 (0.007)	0.0 (0.0)	16.53 (2.31)	15 (10.9)
	45.0	22.5	0.0	0.0	-	15
	Cartesian, MSQP	7.5	5.3	0.39	0.64	19.8
15.0		11.85	0.4	0.61	11.8	6.5
28.0		19.2	0.19	0.33	13.8	6.5
42.0		25.8	0.0	0.0	-	6.5
Cartesian, MOV	18.0	5.4	0.36 (0.49)	0.61 (0.66)	38.7 (38.7)	6.5 (10.9)
	40.0	12.8	0.34	0.65	42.3	10.9
	60.0	19.6	0.002	0.012	11.1	10.9
	80.0	26.2	0.0 (10^{-3}) [†]	0.0 (1.3×10^{-3}) [†]	- (2.0) [†]	10.9 (15) [†]
	100.0	32.2	0.0	0.0	-	10.9
	(cooling/heating also in $ z \leq 1$ kpc)	80.0 [†]	26.2 [†]	0.18 [†]	0.32 [†]	26.4 [†]
					$r_{\text{cold,max}}$ (code units)	runs till (code units)
Cartesian, idealized MSQP (isentropic) (same as McCourt et al. 2012 ; Eqs. 10a-b)	-	0.11	0.85	0.14	2.0	180
	-	0.37	0.66	0.01	2.0	180
	$z_{\text{in}}, z_{\text{out}} = -2, 2$	1.1	0.29	2.4×10^{-4}	2.0	180
	$\Lambda = \Lambda_0 T^{1/2}$ and cuts-off to 0 below 0.05 times the initial midplane temperature;	3.33	0.1	0.0	0.49	180
	$t_{\text{TI}}/t_{\text{ff}}$ is controlled by changing Λ_0	6.6	0.004	0.0	0.53	180
	-	11.0	0.0	0.0	-	180
Cartesian, idealized MSQP (isothermal) (same as McCourt et al. 2012 ; Eq. 9)	-	0.094	0.89	0.28	2.0	180
	-	0.31	0.78	0.08	2.0	180
	$z_{\text{in}}, z_{\text{out}} = -2, 2$	0.94	0.37	0.003	1.7	180
	$\Lambda = \Lambda_0 T^{1/2}$ and cuts-off to 0 below 0.05 times the initial midplane temperature;	2.8	0.06	0.0	0.9	180
	$t_{\text{TI}}/t_{\text{ff}}$ is controlled by changing Λ_0	5.6	0.01	0.0	0.2	180
	-	9.4	1.2×10^{-4}	0.0	0.2	180
-	13.1	0.0	0.0	-	180	

Notes: ^a The ratio of time-averaged cold gas mass and total gas mass within $1\text{kpc} \leq r \leq r_{\text{cold,max}}$. $r_{\text{cold,max}}$ is the maximum distance from the center (at all times) at which cold gas is observed. Some simulations are run for 6.5 and 10.9 Gyr because they take very long; for a uniform comparison the same run is sometimes analyzed till different times.

^b The ratio of time-averaged cold gas mass and total gas mass within $0.9H$ and $1.1H$ (H corresponds to $\min[t_{\text{TI}}/t_{\text{ff}}]$).

[‡] The fiducial NFW runs.

[†] MOV runs with and without heating and cooling at $|z| \leq 1$.

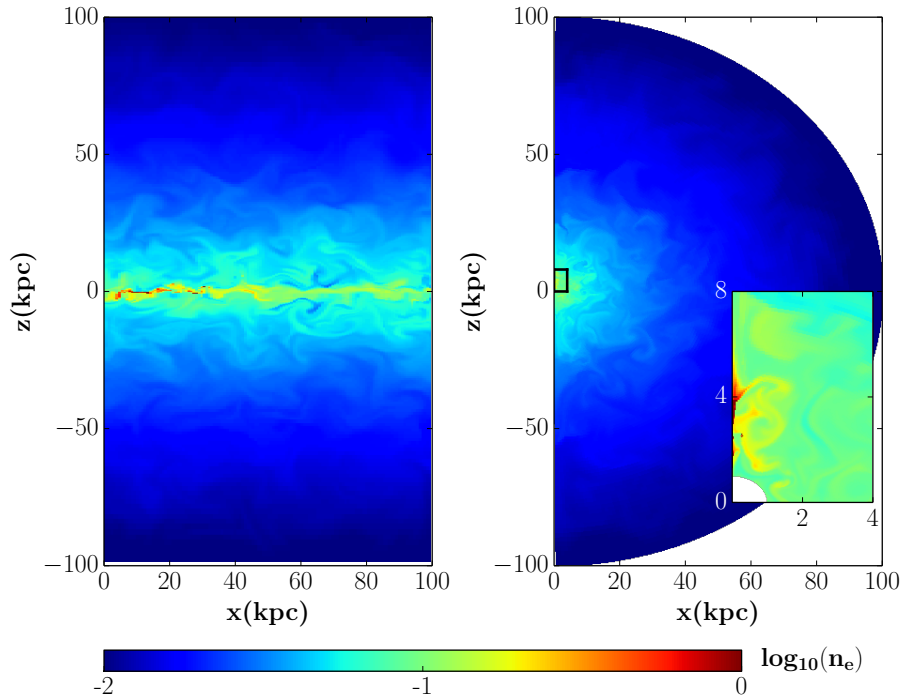


Figure 8. The electron number density snapshots at 1 Gyr (just when cold gas starts to condense) for NFW runs with $\min(t_{\text{T1}}/t_{\text{ff}}) \approx 7.3$ in the equilibrium (unperturbed) profiles. *Left panel:* plane-parallel atmosphere (only half of the horizontal extent is shown); *Right panel:* spherical atmosphere. The inset in the right panel shows the zoomed-in view to highlight the cold gas in the spherical simulation. A key difference between the two setups is that the mass of the cooler gas, out of which cold gas condenses, is much smaller in the spherical atmosphere because of geometry.

4.2 Influence of geometry: results from NFW runs

In this section we compare the results from spherical and plane-parallel NFW simulations to assess the role of geometry on cold gas condensation. As with global linear analysis in section 3.3, numerical simulations show only minor differences between spherical and Cartesian runs.

Figure 8 shows the electron number density snapshots at 1 Gyr, just at the beginning of cold gas condensation in our fiducial NFW simulations ($K_0 = 8 \text{ keV cm}^2$, $\min(t_{\text{T1}}/t_{\text{ff}}) = 7.3$). The key difference between the plane-parallel and spherical atmospheres is that the former has a much larger volume of dense gas out of which cold gas can condense (the volume prone to condensation in Cartesian setup is $2r_{\text{cold,max}}[100 \text{ kpc}]^2$, much larger than in spherical geometry $[4\pi/3]r_{\text{cold,max}}^3$; $r_{\text{cold,max}}$ is the radius/height within which condensation occurs). This results in a much larger amount of cold gas condensing in plane-parallel atmospheres. While cold gas is easily seen in the midplane of the Cartesian setup, it is only seen in the zoomed-in inset for the spherical setup.

Figure 9 shows the zoomed-in electron density snapshots for the Cartesian and spherical runs at times when there is significant cold gas present in the midplane of the plane-parallel run. One can see infalling cold/dense gas condensing out of the hot atmosphere and rising low density plumes; this is very prominent in the Cartesian run. Extended condensation is suppressed later because the dense hot gas has been depleted and has accumulated at the center. Depletion of hot gas density is much more prominent in the Cartesian setup as large amount of cold gas condenses

out and our ansatz of heating balancing cooling overheats the upper layers. Condensation is much smaller in spherical geometry because the volume of gas susceptible to cooling is smaller and there is a huge mass reservoir available to compensate for mass dropout in the core. While the amount of cold gas condensing out strongly depends on geometry, the $\min(t_{\text{T1}}/t_{\text{ff}})$ threshold for both in situ and anywhere condensation is insensitive to it.

4.2.1 Growth rate of perturbations from simulations

Figure 10 shows the growth of density fluctuations at $\min(t_{\text{T1}}/t_{\text{ff}})$ for the fiducial NFW run (with smaller density perturbations) in spherical and Cartesian geometries. The perturbations in $0.9 - 1.1H$ (H corresponds to $\min t_{\text{T1}}/t_{\text{ff}}$ in the equilibrium profile) grow roughly at the *local* thermal instability timescale (t_{T1} ; see Eq. 9). More importantly, the exponential growth rate at early times is similar for spherical and plane-parallel atmospheres. This is consistent with global linear stability analysis of section 3. Therefore, the apparent ease of condensation in a spherical atmosphere as compared to a plane-parallel one cannot be due to a difference in the linear growth rates. The non-linear saturated state shows larger fluctuations in a plane-parallel geometry because of large density perturbations propagating away from the midplane (see section 4.3). The amount of cold gas condensing (both in situ and anywhere) by 15 Gyr and the maximum radius/height till which cold gas exists ($r_{\text{cold,max}}$) are similar for these small amplitude runs are similar to the fiducial run with ≈ 30 times larger density perturbations

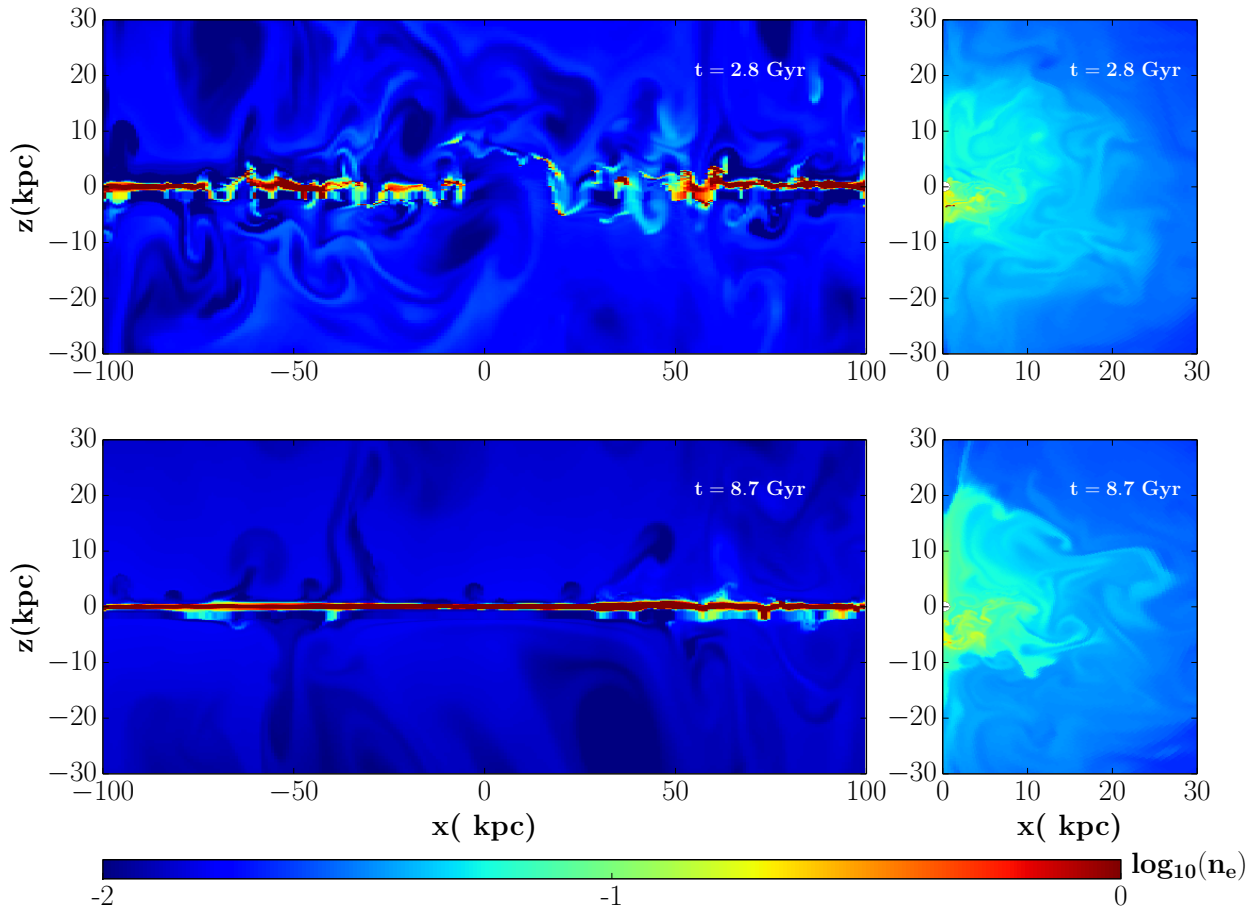


Figure 9. Snapshots of electron number density at two times for plane-parallel (*left*) and spherical (*right*) fiducial NFW runs; early times when there is extended cold gas in the plane-parallel setup and late times when most cold gas is in the midplane. A key difference between the two setups is that the center is excised in the spherical runs, but cold gas has nowhere to go except accumulate at the center in Cartesian runs. Also, the hot gas density is much lower for Cartesian setup as compared to spherical.

(lister in Table 2), implying that the magnitude of initial density perturbations (as long as $\delta\rho/\rho < 1$) does not affect the results over long times.

4.2.2 Cold gas fraction: *in situ* versus condensation anywhere

It is useful to distinguish cold gas which condenses *in situ* at $\min(t_{\text{TI}}/t_{\text{ff}})$ and cold gas which condenses *anywhere* in the box (typically within $\min[t_{\text{TI}}/t_{\text{ff}}]$). It is sensible to make such a distinction both in theory (McCourt et al. 2012) and observations (e.g., McDonald et al. 2010). While centrally concentrated cold gas is associated with the interstellar medium of the central galaxy, extended cold gas is condensing out of the ICM now and falling toward the center (unless uplifted by jets or bubbles).

Figure 11 shows the average cold mass fraction, defined as the ratio of cold ($T < 0.01$ keV) gas mass and the total gas mass between 1 kpc and $r_{\text{cold,max}}$ (the largest radius, over all times, at which cold gas is seen), for several plane-parallel and spherical NFW simulations. The value of $\min(t_{\text{TI}}/t_{\text{ff}})$ is tuned by changing K_0 in Eq. 8. The cold mass fraction is calculated as follows. First, we calculate $r_{\text{cold,max}}$, the max-

imum radius out to which cold gas is detected in all the snapshots (more than 100 over the duration of the run). After that we calculate the average cold gas mass for all snapshots within $1 \text{ kpc} \leq r \leq r_{\text{cold,max}}$ ($1 \text{ kpc} \leq |z| \leq r_{\text{cold,max}}$ for plane-parallel runs) and we divide it by the average total gas mass within the same volume. This way, we somewhat normalize for the fact that there is a much larger volume of dense gas for the plane-parallel setup.

Figure 11 shows that there is only a minor difference in the onset of cold gas condensation for spherical and plane-parallel simulations. For both, there is negligible *in situ* (within $0.9 - 1.1H$, where H corresponds to the radius of $\min[t_{\text{TI}}/t_{\text{ff}}]$) condensation for $\min(t_{\text{TI}}/t_{\text{ff}}) > 8$. Cold gas does condense out at smaller radii for somewhat larger initial $\min(t_{\text{TI}}/t_{\text{ff}}) \approx 18$ in Cartesian geometry. However, there is no cold gas present anywhere for even larger $\min(t_{\text{TI}}/t_{\text{ff}})$, corresponding to a lower density (see Table 2). As expected, a more massive and extended cold gas condensation happens for the runs with a smaller $\min(t_{\text{TI}}/t_{\text{ff}})$. In both geometries, cold mass fraction over the whole box (as opposed to *in situ* condensation) falls slowly as a function of $\min(t_{\text{TI}}/t_{\text{ff}})$. For both geometries, the critical $t_{\text{TI}}/t_{\text{ff}}$ for condensation any-

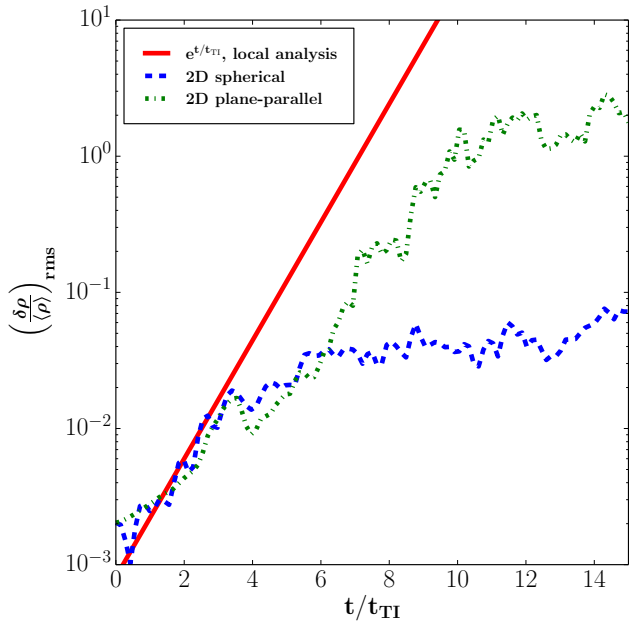


Figure 10. The amplitude of rms density fluctuations $(\delta\rho/\langle\rho\rangle)_{\text{rms}}$, where $\delta\rho = \rho - \langle\rho\rangle$ and $\langle\rangle$ represents shell averaging) measured between $0.9 - 1.1H$ (H is the radius/height corresponding to $\min[t_{\text{TI}}/t_{\text{ff}}]$ in the unperturbed equilibrium state) as a function of time for the fiducial spherical and Cartesian NFW runs with initial $\min(t_{\text{TI}}/t_{\text{ff}}) = 7.3$. The red solid line shows the expected linear growth for modes growing at the local thermal instability timescale (measured at H). The measured growth rates are similar for spherical and Cartesian simulations, and comparable to the local growth rate. To have a significant linear regime, the maximum amplitude of density perturbations in these runs is 0.01 (for other runs it is 0.3).

where in the box is within a factor of two of the critical value for in situ condensation.

4.3 Triggered condensation

Figure 11 shows that condensation anywhere in the simulation box can occur for a larger value of $\min(t_{\text{TI}}/t_{\text{ff}})$ as compared to in situ condensation. Overdense blobs generated at $\min(t_{\text{TI}}/t_{\text{ff}})$ can fall in and induce large perturbations toward the center, and can lead to condensation there even if $t_{\text{TI}}/t_{\text{ff}}$ is larger than its value at the minimum.

Figure 9 shows a big difference in the state of the hot gas; namely, the hot gas density in plane-parallel simulation is much smaller than in the spherical run. To quantitatively study the state of the hot gas, in Figure 12 we plot the shell-averaged $t_{\text{TI}}/t_{\text{ff}}$ of the hot gas ($T > 0.1$ keV) at different times for the spherical and plane-parallel fiducial runs with initial $\min(t_{\text{TI}}/t_{\text{ff}}) = 7.3$. For spherical simulations, excess gas is removed from the hot phase in form of cold filaments, and the ICM settles with $\min(t_{\text{TI}}/t_{\text{ff}}) \gtrsim 10$, as also found in [Sharma et al. \(2012b\)](#). In contrast, the outer regions in the plane-parallel simulation get evacuated at later times due to plenty of hot bubbles rising from the innermost layers and displacing the denser gas. These rising low density

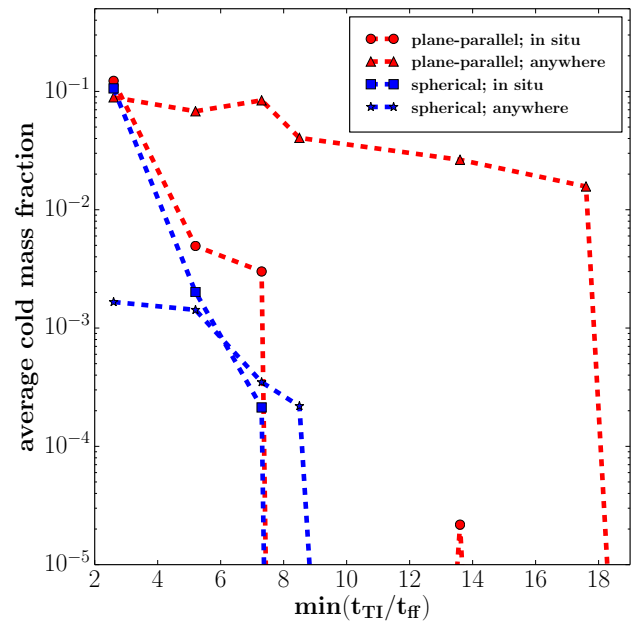


Figure 11. The ratio of average (over 15 Gyr) cold ($T < 0.01$ keV) gas mass to the average total mass (in situ and anywhere) for various values of initial $\min(t_{\text{TI}}/t_{\text{ff}})$ for the spherical and plane-parallel NFW runs. While there is essentially no cold gas condensation for spherical runs with $\min(t_{\text{TI}}/t_{\text{ff}}) > 8$, cold gas condenses out at smaller heights for plane-parallel runs with $\min(t_{\text{TI}}/t_{\text{ff}}) \lesssim 18$.

gas plumes create large density perturbations ($\delta\rho/\rho \gtrsim 1$; see late times in Fig. 10) and trigger further condensation (note that the $\min[t_{\text{TI}}/t_{\text{ff}}]$ threshold applies only for small density perturbations; cold gas can condense out from lower density atmospheres if density perturbations are large), explaining the presence of central cold gas for higher $\min(t_{\text{TI}}/t_{\text{ff}})$ in Figure 11 for plane-parallel simulations compared to spherical. The hot gas is evacuated from most of the volume, with $\min(t_{\text{TI}}/t_{\text{ff}})$ at late times significantly larger than the critical value of 10, and cold gas settles down in the midplane (see Fig. 9). Evacuation of gas away from the midplane is partly because of our imposed thermal balance in layers. As gas cools through 10^7 to 10^4 K the rise in the cooling function results in excessive heating and thermal transport to upper layers. In the realistic spherical atmosphere the outer layers are least affected by the tiny hot bubbles rising from the core region because the mass of cold gas condensing is much smaller.

4.4 Condensation with different densities and gravities: plane-parallel runs

While we have convincingly shown that geometry does not play a key role in determining condensation properties in our setup, we also want to assess the role of gravitational acceleration and equilibrium entropy/density profiles in cold gas condensation. Various astrophysical coronae (e.g., accretion disk and galactic coronae; [Das & Sharma 2013](#); [Joung, Bryan & Putman 2012](#); [Sharma et al. 2012a](#)) have different distri-

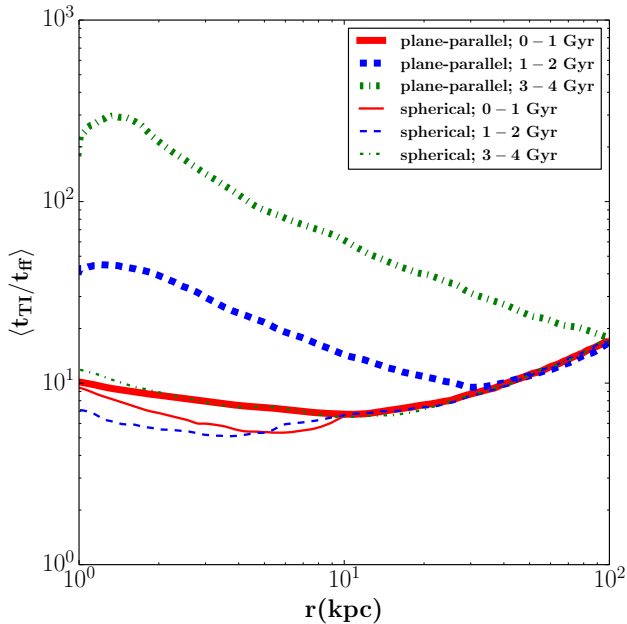


Figure 12. Evolution of shell-averaged $t_{\text{TI}}/t_{\text{ff}}$ (averaged over different times) for hot gas ($T > 0.1$ keV) in fiducial spherical and plane-parallel NFW runs. This ratio is much larger at late times for plane-parallel runs, implying that hot plumes move up and displace denser gas from there (see also Fig. 9). In spherical atmosphere condensation does not affect the overlying layers as much.

butions of gravitational accelerations and hot gas densities, and the details of cold gas formation may differ.

In order to compare with [McCourt et al. \(2012\)](#), Figure 13 shows the in situ and anywhere cold mass fraction for idealized isothermal and isentropic MSQP runs in Cartesian geometry. Both gravity and density/temperature profiles are different for these runs as compared to the NFW runs (see Fig. 7). However, the results are qualitatively similar; there is a cut-off $\min(t_{\text{TI}}/t_{\text{ff}})$ beyond which no cold gas condenses, either in situ at $\min(t_{\text{TI}}/t_{\text{ff}})$ (critical value ≈ 1) or anywhere in the simulation domain (critical value ≈ 8). A smaller threshold of $t_{\text{TI}}/t_{\text{ff}}$ for idealized MSQP runs (especially for in situ condensation) as compared to NFW runs can be understood from the shapes of $t_{\text{TI}}/t_{\text{ff}}$ profiles in Figure 7. Going toward the center, this ratio rises more steeply for idealized MSQP runs as compared to NFW runs. This means that there is a much larger volume prone to condensation for NFW atmospheres in contrast to the idealized MSQP ones, leading to the relative ease of condensation in former. There is no significant difference between condensation in isothermal and isentropic idealized atmospheres, implying that background entropy stratification does not play a critical role in nonlinear evolution.

Figure 14 shows the average cold mass fraction (both in situ and anywhere) as a function of $\min(t_{\text{TI}}/t_{\text{ff}})$ for similar initial entropy profiles (Eq. 8) but for NFW and MOV/MSQP gravities (Eqs. 5, 6/7). The noticeable differences between the NFW and MOV/MSQP gravities are that the amount of cold gas condensing is higher for

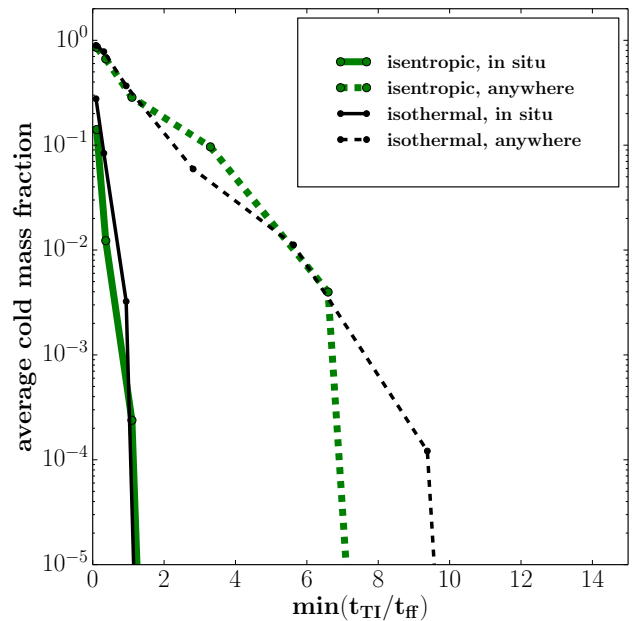


Figure 13. The ratio of average (over 180 code units) cold mass ($T \leq T_0/10$) to the average total mass as a function of $\min(t_{\text{TI}}/t_{\text{ff}})$ for idealized isothermal/isentropic Cartesian MSQP runs. The average cold mass fraction, for both in situ ($0.9 - 1.1H$) and anywhere ($|z| < 0.1$ is excluded) condensation, is qualitatively similar to Fig. 11 for NFW runs. However, the $t_{\text{TI}}/t_{\text{ff}}$ threshold for condensation anywhere is a factor of ≈ 7 larger than in situ condensation.

MOV/MSQP, and that the threshold for in situ and anywhere condensation are similar for MOV/MSQP but differ by about a factor of two for NFW. In fact, the in situ cold fraction is higher for MOV/MSQP profiles that have $\min(t_{\text{TI}}/t_{\text{ff}})$ at the center. For profiles with $\min(t_{\text{TI}}/t_{\text{ff}})$ away from the center (e.g., NFW), cold gas condensation is seeded far away from the center but eventually happens much closer in. For $\min(t_{\text{TI}}/t_{\text{ff}})$ at the center, cold gas condensation is anyway most efficient at the center.

Figure 15 shows cold gas mass fraction as a function of time for Cartesian runs with NFW, MOV, and MSQP gravities with initial $\min(t_{\text{TI}}/t_{\text{ff}}) \approx 5$; the corresponding $t_{\text{TI}}/t_{\text{ff}}$ and density profiles are shown in Figure 7. Figure 7 shows that the central density of MSQP model is the largest. Therefore, cold gas condenses out earliest in this model. The $t_{\text{TI}}/t_{\text{ff}}$ profiles are quite similar for MSQP and MOV models. Cold gas condenses out almost simultaneously for MSQP and NFW models because of a similar density (and hence the cooling time) at the location of $\min(t_{\text{TI}}/t_{\text{ff}})$. While the cold gas fraction (also the cold gas mass) is higher and attains an almost constant level for MOV and MSQP models in Figure 15, it is smaller and decreases gradually for the NFW model. This is very likely due to the qualitatively different $t_{\text{TI}}/t_{\text{ff}}$ profiles for NFW as compared to MOV and MSQP atmospheres. With a $t_{\text{TI}}/t_{\text{ff}}$ minimum away from the center, the gas close to the center is not prone to multiphase cooling.

The comparison of average cold fraction, both in situ and anywhere, for MSQP gravity in Figures 13 and 14 shows

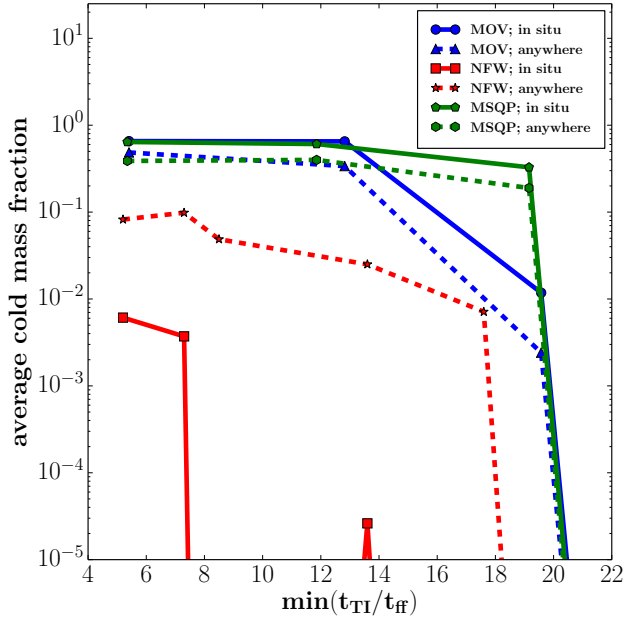


Figure 14. Average cold gas mass fraction (over 10.9 Gyr) for plane-parallel MOV and NFW runs (also shown are results from MSQP runs averaged over 6.5 Gyr) for different initial $\min(t_{\text{TI}}/t_{\text{FF}})$. While the in situ and anywhere condensation ratio is very similar for MOV and MSQP runs, the threshold $\min(t_{\text{TI}}/t_{\text{FF}})$ for in situ condensation in NFW runs is a factor of about two smaller as compared to condensation anywhere in the box. Note that unlike NFW runs, in situ cold mass fraction is larger than anywhere cold mass fraction for MOV/MSQP runs.

that the condensation properties are essentially a function of the value and shape of $t_{\text{TI}}/t_{\text{FF}}$ profiles (and not just gravity or density profiles). Profiles with a minimum far away from the center (NFW and idealized MSQP; see Fig. 7) show lower amount of cold gas and a larger difference between the critical threshold for in situ and anywhere condensation.

4.5 Enhanced condensation in midplane with no gravity

Based on their simulations, Meece, O’Shea & Voit (2015) have recently argued that there is no threshold of $t_{\text{TI}}/t_{\text{FF}}$ for condensation to occur. That is, condensation will always occur, provided one waits long enough. This conclusion differs from the claim of McCourt et al. (2012), who turn off cooling and heating at the midplane of the simulation domain. While $t_{\text{TI}}/t_{\text{FF}}$ for MOV and MSQP gravities formally has a finite value as $z \rightarrow 0$, gas in thermal balance at the midplane is essentially unaffected by gravity and will become multiphase over a cooling time for all cases. This is what leads to the formation of substantial quantities of cold gas in the simulations of Meece, O’Shea & Voit (2015) even if $\min(t_{\text{TI}}/t_{\text{FF}}) \gtrsim 30$.

Figure 16 shows a comparison of the Cartesian MOV simulations, with an initial $\min(t_{\text{TI}}/t_{\text{FF}})=26.2$, with (right panel) and without (left panel) heating/cooling turned off in the midplane ($|z| < 1$ kpc). A comparison of the two panel

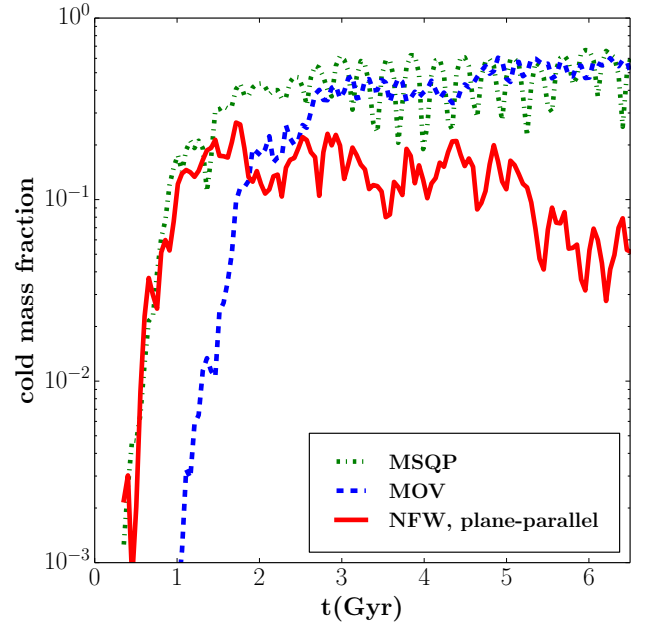


Figure 15. Comparison of onset time and cold mass fraction as a function of time for Cartesian runs with NFW (with equilibrium $\min[t_{\text{TI}}/t_{\text{FF}}] = 5.2$), MOV ($\min[t_{\text{TI}}/t_{\text{FF}}] = 5.4$) and MSQP ($\min[t_{\text{TI}}/t_{\text{FF}}] = 5.3$) gravities. Cold mass fraction is higher for MOV and MSQP runs as compared to the NFW run, which also shows a slow decline with time.

clearly shows that there is much more cold gas condensing out in the latter case. Condensation occurs even beyond the midplane; this is seeded by perturbations generated at the midplane and by cold gas rising up due to buoyant hot bubbles. Table 2 also shows a much larger cold gas fraction for the run that allows cooling and heating in the midplane. Thus, turning off multiphase gas production in the midplane is necessary to carefully assess the source of extended cold gas in cool cluster cores.

5 CONCLUSIONS

We have used global linear analysis and idealized numerical simulations in global thermal balance to address the question of cold gas condensation in cool cluster cores and other astrophysical coronae. We have not varied all the parameters in our simulations because earlier works had explored those (e.g., a comparison of 2-D and 3-D and the effect of small initial density perturbations). Particular attention is paid to the influence of geometry and the profile of the ratio of the cooling time to the free-fall time ($t_{\text{cool}}/t_{\text{FF}}$). We have used different forms of gravities (Fig. 1) and hydrostatic atmospheres (Figs. 5 & 7) to carry out our investigations. Previous works (except for the recent paper of Meece, O’Shea & Voit 2015) somewhat erroneously assumed that it was easier for cold gas to condense out in spherical geometry as compared to a plane-parallel atmosphere. The key reason for this confusion was that McCourt et al. (2012) focused on in situ condensation of cold gas but Sharma et al. (2012b)

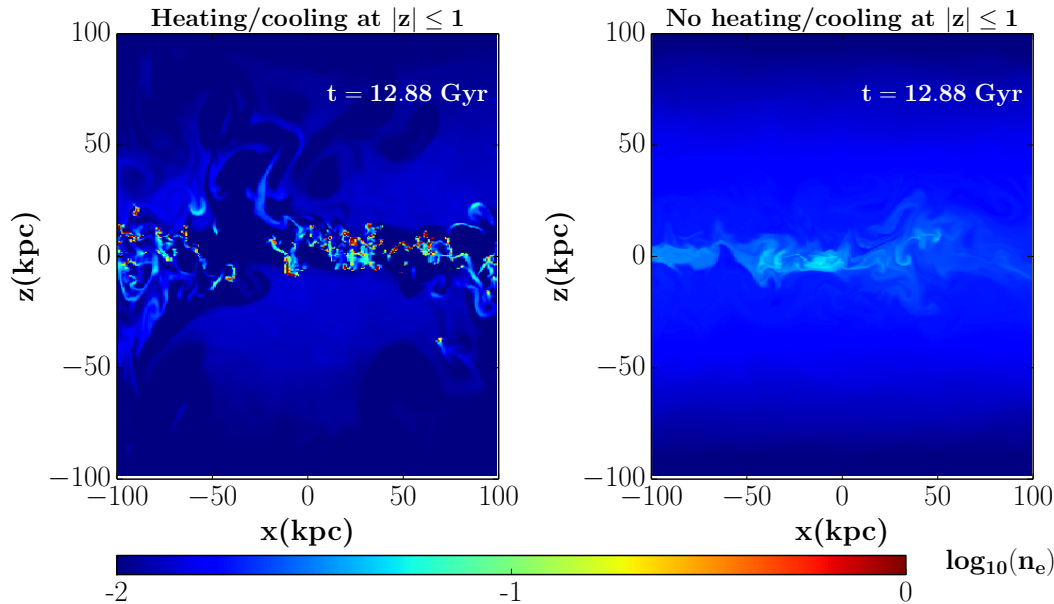


Figure 16. Electron number density snapshots for MOV Cartesian runs with (left panel) and without (right panel) cooling/heating in the midplane ($|z| < 1$). There is widespread multiphase gas with heating and cooling allowed in the midplane.

quantified condensation of cold gas anywhere in the box, not necessarily at the location of the minimum in $t_{\text{cool}}/t_{\text{ff}}$.

The main conclusions of our paper are:

- *Linear growth rate of global modes is independent of geometry and gravity:* Global linear analysis shows that the growth rate of the global modes is the same for spherical and Cartesian geometries (Fig. 6). This is also verified in numerical simulations by measuring the density growth in the two geometries (Fig. 10). Moreover, the growth rate of global modes is similar to the local isobaric thermal instability growth rate. Therefore, any differences observed for condensation in different geometries and gravities are due to nonlinear effects such as seeding of condensation due to rising/sinking underdense/overdense blobs.

- *Critical $\min(t_{\text{TI}}/t_{\text{ff}})$ is essentially independent of geometry but much higher cold gas condenses in plane-parallel geometry:* Cold gas condensation, in our simulations with small density perturbations, occurs only if $t_{\text{TI}}/t_{\text{ff}}$ is smaller than a critical value close to 10. Our plane-parallel NFW simulations show that much more cold gas condenses out of the hot phase compared to spherical simulations (Fig. 9). This is because of the much bigger volume which is prone to multiphase condensation for the former. A large amount of multiphase gas leads to strong heating (because of thermal balance ansatz), and large fluctuations lead to the condensation of a lot of gas, even in regions where $t_{\text{TI}}/t_{\text{ff}} > 10$. For realistic spherical runs, on the other hand, only a small volume is prone to condensation and the fluctuations induced due to this are not sufficient to affect the overlying gas with $t_{\text{TI}}/t_{\text{ff}} > 10$ (right panels of Fig. 9). The *onset* of cold gas condensation, both in situ where $t_{\text{TI}}/t_{\text{ff}}$ is minimum and anywhere in the box, happens at a similar value of threshold $\min(t_{\text{TI}}/t_{\text{ff}})$ for spherical and plane-parallel setups (Fig. 11).

- *Role of $t_{\text{TI}}/t_{\text{ff}}$ profile:* The gravity and gas density pro-

files, via the dimensionless ratio $t_{\text{TI}}/t_{\text{ff}}$ (the ratio of local thermal instability timescale and the free-fall time), play a crucial role in governing cold gas condensation. In cases where $\min(t_{\text{TI}}/t_{\text{ff}})$ is far away from the center (e.g., NFW, idealized MSQP; see Fig. 7), the $\min(t_{\text{TI}}/t_{\text{ff}})$ threshold for in situ condensation is considerably smaller compared to the threshold for condensation anywhere (Figs. 11, 13). For MOV and MSQP profiles (Fig. 7), for which $\min(t_{\text{TI}}/t_{\text{ff}})$ lies at the center, there is essentially no difference between in situ and condensation anywhere (see Fig. 14). For idealized MSQP and NFW profiles, with $\min(t_{\text{TI}}/t_{\text{ff}})$ away from the center, overdense gas falling in from $\min(t_{\text{TI}}/t_{\text{ff}})$ triggers (nonlinearly) condensation toward the center where $(t_{\text{TI}}/t_{\text{ff}})$ is larger. Atmospheres with weaker gravity at the center, such as MOV (see Fig. 1), allow fluctuations arising at the center (where there is multiphase cooling) to larger heights where they can trigger cooling, leading to multiphase condensation at greater heights ($r_{\text{cool,max}}$ is larger for MOV runs in Table 2).

- *Triggered multiphase gas due to large density perturbations:* Large density perturbations can give rise to the condensation of multiphase gas even if $t_{\text{cool}}/t_{\text{ff}}$ is larger than the critical value (e.g., Fig. 7 in Singh & Sharma 2015). This is what happens at the center of NFW runs which do not show in situ condensation at $\min(t_{\text{cool}}/t_{\text{ff}})$ but toward the center. Large overdensities generated at $\min(t_{\text{cool}}/t_{\text{ff}})$ propagate inward and lead to cold gas condensation at smaller radii. Similarly, for plane-parallel runs, density fluctuations originating close to $\min(t_{\text{cool}}/t_{\text{ff}})$ propagate outwards and lead to widespread dropout as compared to a realistic spherical geometry of the ICM. A dramatic example of triggered multiphase condensation is shown in Figure 16 which compares two MOV plane-parallel simulations in one of which cooling/heating is allowed in the midplane. Since the gas in the midplane does not experience any gravity, cold gas

condenses out in the midplane and the large density perturbations generated there trigger condensation far away from the center. Meece, O'Shea & Voit (2015) do not turn off heating and cooling at the center and therefore their results are strongly affected by condensation triggered due to density fluctuations propagating away from the midplane. This is the reason they do not see a $\min(t_{\text{cool}}/t_{\text{ff}})$ threshold for condensation in their simulations.

Our key result is that cold gas condensation, starting with small amplitude perturbations, is expected only if $\min(t_{\text{TI}}/t_{\text{ff}}) \lesssim 10$. This result is only weakly sensitive to the gravitational potential and density/temperature profiles. It is not possible to understand this threshold from linear physics arguments. Nonlinear effects, such as triggering of multiphase condensation due to motion of overdense/underdense blobs across layers, play important role in explaining the results from various idealized numerical simulations.

ACKNOWLEDGEMENTS

This work is partly supported by the DST-India grant no. Sr/S2/HEP-048/2012 and an India-Israel joint research grant (6-10/2014[IC]). We thank Matt Kunz for sharing the code that was used in Latter & Kunz (2012). We also thank Ramesh Narayan for useful discussions on the global linear stability analysis.

REFERENCES

- Balbus S. A., 1988, *ApJ*, 328, 395
 Balbus S. A., Soker N., 1989, *ApJ*, 341, 611
 Banerjee N., Sharma P., 2014, *MNRAS*, 443, 687
 Bower R. G., Benson A. J., Malbon R., Helly J. C., Frenk C. S., Baugh C. M., Cole S., Lacey C. G., 2006, *MNRAS*, 370, 645
 Boyd, J. P., 2000, *Chebyshev and Fourier Spectral Methods*. Dover Publications, p. 109
 Cavagnolo K. W., Donahue M., Voit G. M., Sun M., 2009, *ApJS*, 182, 12
 Das U., Sharma P., 2013, *MNRAS*, 435, 2431
 Field G. B., 1965, *ApJ*, 142, 531
 Gaspari M., Ruszkowski M., Sharma P., 2012, *ApJ*, 746, 94
 Hayes J. C., Norman M. L., Fiedler R. A., Bordner J. O., Li P. S., Clark S. E., ud-Doula A., Mac Low M.-M., 2006, *ApJS*, 165, 188
 Joung M. R., Bryan G. L., Putman M. E., 2012, *ApJ*, 745, 148
 Kim W.-T., Narayan R., 2003, *ApJ*, 596, 889
 Latter H. N., Kunz M. W., 2012, *MNRAS*, 423, 1964
 Li Y., Bryan G. L., 2014, *ApJ*, 789, 153
 Li Y., Bryan G. L., Ruszkowski M., Voit G. M., O'Shea B. W., Donahue M., 2015, *ApJ*, 811, 73
 Lufkin E. A., Balbus S. A., Hawley J. F., 1995, *ApJ*, 446, 529
 Malagoli A., Rosner R., Bodo G., 1987, *ApJ*, 319, 632
 McCourt M., Sharma P., Parrish I. J., Quataert E., 2012, *MNRAS*, 419, 3319
 McDonald M., Veilleux S., Rupke D. S. N., Mushotzky R., 2010, *ApJ*, 721, 1262
 McNamara B. R., Nulsen P. E. J., 2007, *ARA&A*, 45, 117
 Meece G. R., O'Shea B. W., Voit G. M., 2015, *ApJ*, 808, 43
 Navarro J. F., Frenk C. S., White S. D. M., 1996, *ApJ*, 463, 563
 Parrish I. J., Quataert E., Sharma P., 2009, *ApJ*, 703, 96
 Pizzolato F., Soker N., 2005, *ApJ*, 632, 821
 Prasad D., Sharma P., Babul A., 2015, *ApJ*, 811, 108
 Rafferty D. A., McNamara B. R., Nulsen P. E. J., 2008, *ApJ*, 687, 899
 Sharma P., McCourt M., Parrish I. J., Quataert E., 2012a, *MNRAS*, 427, 1219
 Sharma P., McCourt M., Quataert E., Parrish I. J., 2012b, *MNRAS*, 420, 3174
 Sharma P., Parrish I. J., Quataert E., 2010, *ApJ*, 720, 652
 Singh A., Sharma P., 2015, *MNRAS*, 446, 1895
 Springel V. et al., 2005, *Nature*, 435, 629
 Voit G. M., Donahue M., Bryan G. L., McDonald M., 2015, *Nature*, 519, 203
 Wagh B., Sharma P., McCourt M., 2014, *MNRAS*, 439, 2822
 White S. D. M., Frenk C. S., 1991, *ApJ*, 379, 52

APPENDIX A: GLOBAL LINEAR EQUATIONS IN SPHERICAL COORDINATES

The perturbed quantities in Eqs. 12-16 can be expanded using a spherical harmonic basis as follows,

$$\rho_1 = R_\rho Y_l^m, p_1 = R_p Y_l^m, s_1 = R_s Y_l^m, T_1 = R_T Y_l^m,$$

$$v_{r1} = R_r Y_l^m, v_{\theta 1} = R_\theta \frac{\partial Y_l^m(\theta, \phi)}{\partial \theta}, v_{\phi 1} = \frac{R_\phi}{\sin \theta} \frac{\partial Y_l^m(\theta, \phi)}{\partial \phi},$$

where $Y_l^m(\theta, \phi)$ is the spherical harmonic of order (l, m) and R carries the radial dependence. These forms are obtained by comparing the r, θ, ϕ dependence of various terms in Eqs. 12-16, which also imply that $R_\phi = R_\theta$. The equations become

$$\sigma R_\rho = -\frac{1}{r^2} \frac{d}{dr} (r^2 \rho_0 R_r) + l(l+1) \frac{\rho_0 R_\theta}{r}, \quad (\text{A1})$$

$$\sigma R_r = -\frac{1}{\rho_0} \frac{d}{dr} \left[p_0 \left(\frac{R_s}{s_0} + \gamma \frac{R_\rho}{\rho_0} \right) \right] - \frac{g R_\rho}{\rho_0}, \quad (\text{A2})$$

$$\sigma R_\theta = -\frac{p_0}{r \rho_0} \left(\frac{R_s}{s_0} + \gamma \frac{R_\rho}{\rho_0} \right), \quad (\text{A3})$$

$$\begin{aligned} \sigma R_s &= \frac{\gamma s_0 N^2}{g} R_r \\ &- \frac{s_0}{t_{\text{cool}0}} \left[2 \frac{R_\rho}{\rho_0} + \frac{d \ln \Lambda}{d \ln T} \left(\frac{R_s}{s_0} + (\gamma - 1) \frac{R_\rho}{\rho_0} \right) \right]. \end{aligned} \quad (\text{A4})$$

The local forms (assuming $e^{ik_x x}$ dependence; x is the local coordinate along θ) of Eqs. 12 - 16 are

$$\sigma \rho_1 + \frac{1}{r^2} \frac{\partial}{\partial r} (r^2 \rho_0 v_{r1}) + ik_x \rho_0 v_{x1} = 0, \quad (\text{A5})$$

$$\sigma \rho_0 v_{r1} = -\frac{\partial p_1}{\partial r} - \rho_1 g, \quad (\text{A6})$$

$$\sigma \rho_0 v_{x1} = -ik_x p_1, \quad (\text{A7})$$

$$\sigma \frac{s_1}{s_0} + \frac{\gamma N^2 v_{r1}}{g} = \frac{-1}{t_{\text{cool}0}} \left[2 \frac{\rho_1}{\rho_0} + \frac{d \ln \Lambda}{d \ln T} \frac{T_1}{T_0} \right]. \quad (\text{A8})$$

Both the local (in θ) and global equations can be solved as eigenvalue problems with given parameters l, m (for global setup) or k_x (for local setup). For plane-parallel (as opposed to spherical) global linear analysis we just have to set the second term in Eq. A5 to be $d(\rho_0 v_{z1})/dz$.

APPENDIX B: PSEUDOSPECTRAL METHOD

We use the pseudospectral method (chapters 6 & 7 in Boyd, J. P. 2000; Latter & Kunz 2012) to solve the set of eigen-equations, Eqs. A5-A8 (Eqs. A1-A4 for spherical global $\theta - \phi$ modes), by approximating the eigenfunctions in terms of n Chebyshev polynomials of first kind (T) as:

$$\begin{aligned} \frac{\rho_1}{\rho_0} &= \sum_{j=0}^{n-1} \tilde{\rho}_j T_j(\xi); \quad \frac{v_{r1}}{c_0} = \sum_{j=0}^{n-1} \tilde{v}_{rj} T_j(\xi); \\ \frac{v_{x1}}{c_0} &= \sum_{j=0}^{n-1} \tilde{v}_{xj} T_j(\xi); \quad \frac{s_1}{s_0} = \sum_{j=0}^{n-1} \tilde{s}_j T_j(\xi); \end{aligned} \quad (\text{B1})$$

where $\xi = 2(r - r_{\text{in}})/(r_{\text{out}} - r_{\text{in}}) - 1$ maps the domain going from r_{in} to r_{out} on to $-1 \leq \xi \leq 1$, as Chebyshev polynomials are complete and orthonormal only over this domain.

The radial domain is partitioned into a Gauss-Lobatto grid so that $\xi(i)$ can be generated in the following way

$$\xi[i] = \cos \left(\frac{i\pi}{n-1} \right); \quad r[i] = (\xi[i] + 1) \frac{(r_{\text{out}} - r_{\text{in}})}{2} + r_{\text{in}},$$

where $i = 0, \dots, (n-1)$ denotes the n G-L points. At each $r[i]$, each of the equilibrium profiles of $\rho_0, p_0, s_0, T_0, N^2$ and $t_{\text{cool}0}$ are obtained and we formulate the $4n \times 4n$ (Eqs. A1-A4) matrix eigenvalue problem; some of the rows of the matrix incorporate our boundary conditions (see section 3). Incorporating the above into the differential eigen-system (Eqs. A1-A4 for global spherical modes and Eqs. A5-A8 for local modes), we can convert it into a matrix form so that we get a matrix whose eigenvalues (σ) are the growth rates (or decay rates if real parts are negative; the imaginary parts correspond to oscillation frequencies).

The discretized eigenproblem takes the form (assuming that the repeated index is summed over all possible values)

$$\mathcal{L}_{ij} v_j = \sigma \mathcal{M}_{ij} v_j \quad (\text{B2})$$

where \mathcal{L} and \mathcal{M} are $4n \times 4n$ matrices; i is the radial grid index for dependent variables (ρ_1, v_{r1} , etc.) and j stands for the order of Chebyshev basis for ρ_1, v_{r1} , etc. As a result, we can consider \mathcal{L} and \mathcal{M} to be consisting of 4×4 blocks, each of size $n \times n$. For example, in terms of our dependent variables, Eq. A7 can be written as $\sigma \rho_0 v_{x1} = -ik_x p_0 (\gamma \rho_1 / \rho_0 + s_1 / s_0)$. The discretized equations for v_{x1} correspond to rows from $2n$ to $3n-1$ of Eq. B2; rows $2n$ and $3n-1$ implement the outer and inner boundary conditions. For Eq. A7, Matrix \mathcal{L} will have non-zero entries in columns $j = 0, \dots, n-1$ (corresponding to ρ_1) and $j = 3n, \dots, 4n-1$ (corresponding to s_1), and \mathcal{M} has non-zero entries in columns $j = 2n, \dots, 3n-1$. Once we obtain the eigenvalues and eigenvectors, we substitute them in Eq. B1 to obtain the spatial profiles of eigenmodes. Since our equations and boundary conditions are homogeneous, the amplitude of modes is arbitrary within a multiplicative factor and the real and imaginary components of eigenmodes and eigenvalues can be combined with an arbitrary phase and amplitude, e.g.,

$$\rho_1 = K (\rho_{1r} \sin \phi + \rho_{1i} \cos \phi),$$

where K and ϕ are arbitrary real numbers and $\rho_{1r/i}$ is the real/imaginary part of the density eigenmode. The other complex eigenmodes (e.g., v_{r1r}, v_{r1i}) are combined with the same value of K and ϕ .

As mentioned in Boyd, J. P. 2000, the pseudospectral method gives several spurious eigenvalues and one must perform convergence studies to choose the physically correct modes (e.g., Fig. 2). Also, the higher wavenumber modes are better resolved as we increase the resolution (n).